NeuroImage 189 (2019) 497–515

Contents lists available at ScienceDirect

NeuroImage

journal homepage: www.elsevier.com/locate/neuroimage

Generalized diffusion spectrum magnetic resonance imaging (GDSI) for model-free reconstruction of the ensemble average propagator

Qiyuan Tian [a,b,*], Grant Yang [a,b], Christoph Leuze [b], Ariel Rokem [c], Brian L. Edlow [d,e], Jennifer A. McNab [b]

[a] Department of Electrical Engineering, Stanford University, Stanford, CA, United States
[b] Radiological Sciences Laboratory, Department of Radiology, Stanford University, Richard M. Lucas Center for Imaging, Stanford, CA, United States
[c] eScience Institute, University of Washington, Seattle, WA, United States
[d] Athinoula A. Martinos Center for Biomedical Imaging, Massachusetts General Hospital, Charlestown, MA, United States
[e] Center for Neurotechnology and Neurorecovery, Department of Neurology, Massachusetts General Hospital, Boston, MA, United States

ARTICLE INFO

Keywords:
Q-space imaging
Diffusion spectrum imaging
Ensemble average propagator
Orientation distribution function
Multi-shell acquisition
Sampling density non-uniformity correction
Model-free

ABSTRACT

Diffusion spectrum MRI (DSI) provides model-free estimation of the diffusion ensemble average propagator (EAP) and orientation distribution function (ODF) but requires the diffusion data to be acquired on a Cartesian q-space grid. Multi-shell diffusion acquisitions are more flexible and more commonly acquired but have, thus far, only been compatible with model-based analysis methods. Here, we propose a generalized DSI (GDSI) framework to recover the EAP from multi-shell diffusion MRI data. The proposed GDSI approach corrects for q-space sampling density non-uniformity using a fast geometrical approach. The EAP is directly calculated in a preferable coordinate system by multiplying the sampling density corrected q-space signals by a discrete Fourier transform matrix, without any need for gridding. The EAP is demonstrated as a way to map diffusion patterns in brain regions such as the thalamus, cortex and brainstem where the tissue microstructure is not as well characterized as in white matter. Scalar metrics such as the zero displacement probability and displacement distances at different fractions of the zero displacement probability were computed from the recovered EAP to characterize the diffusion pattern within each voxel. The probability averaged across directions at a specific displacement distance provides a diffusion property based image contrast that clearly differentiates tissue types. The displacement distance at the first zero crossing of the EAP averaged across directions orthogonal to the primary fiber orientation in the corpus callosum is found to be larger in the body (5.65 ± 0.09 μm) than in the genu (5.55 ± 0.15 μm) and splenium (5.4 ± 0.15 μm) of the corpus callosum, which corresponds well to prior histological studies. The EAP also provides model-free representations of angular structure such as the diffusion ODF, which allows estimation and comparison of fiber orientations from both the model-free and model-based methods on the same multi-shell data. For the model-free methods, detection of crossing fibers is found to be strongly dependent on the maximum b-value and less sensitive compared to the model-based methods. In conclusion, our study provides a generalized DSI approach that allows flexible reconstruction of the diffusion EAP and ODF from multi-shell diffusion data and data acquired with other sampling patterns.

1. Introduction

Q-space diffusion magnetic resonance imaging (QSI) provides model-free estimation of the diffusion ensemble average propagator (EAP, also known as spin displacement probability density function and diffusion spectrum) and diffusion orientation distribution function (ODF) only relying on a Fourier relationship between the attenuated echo signal in q-space and the EAP. In the 1960s, Stejskal and Tanner formulated the pulsed gradient spin echo (PGSE) nuclear magnetic resonance (NMR) experiment using the propagator language that Einstein used to formulate Fick's Law (Einstein, 1905; Stejskal and Tanner, 1965). Stejskal and Tanner also proposed to recover the propagator of non-Gaussian diffusion and flow by taking a Fourier transform of signals measured by varying pulsed gradient direction and strength (Stejskal, 1965). To

* Corresponding author. Radiological Sciences Laboratory, Department of Radiology, Stanford University, Richard M. Lucas Center for Imaging, 1201 Welch Road, Stanford, CA, 94305, USA.
E-mail address: qytian@stanford.edu (Q. Tian).

https://doi.org/10.1016/j.neuroimage.2019.01.038
Received 14 April 2018; Received in revised form 6 December 2018; Accepted 14 January 2019
Available online 23 January 2019
1053-8119/

simplify the initial formalism, Kärger and Heink later introduced the concept of the EAP (Kärger and Heink, 1969), which denotes the ensemble probability that spins at any starting position in a heterogeneous system displace by a certain displacement. In the 1980s, the PGSE NMR experiment was extended to MRI (Cory, 1990; Jenner et al., 1988). Callaghan then recast Stejskal and Tanner's formalism in terms of the wave vector, $\boldsymbol{q}$ (Callaghan et al., 1988), and proposed the concept of q-space, in analogy to k-space (Twieg, 1983; Ljunggren, 1969). It was not until the mid-1990s that QSI was introduced to study the central nervous system (King et al., 1994, 1997). In the early 2000s, Assaf and Cohen conducted a series of QSI studies (Cohen and Assaf, 2002) to infer the neuronal structure of bovine optic nerve (Assaf and Cohen, 1999, 2000), rat brain (Assaf and Cohen, 2000) and spinal cord (Assaf et al., 2000), and *in vivo* human brain (Assaf et al., 2002, 2005) from the EAP. Around the same time, Wedeen utilized QSI to delineate intra-voxel crossing fibers (known as diffusion spectrum imaging (DSI) (Wedeen et al., 2000; Wiegell et al., 2001; Lin et al., 2003)) for tracking white matter fiber pathways (i.e. tractography) in the *in vivo* human brain (Conturo et al., 1999; Mori et al., 1999) and proposed a new theory regarding the fundamental geometric structure of hemispheric fiber pathways (Wedeen et al., 2012). One limitation of DSI is that it only recovers the EAP and the diffusion ODF from q-space data acquired on a 3-dimension (3D) Cartesian grid. Here, we generalize the Cartesian DSI method by proposing a flexible framework that is also compatible with non-Cartesian (e.g. multi-shell) q-space data.

Even though the ODF is of great interest for tractography purposes, the EAP provides additional information of the tissue microstructure beyond fiber orientations. The EAP was found to be sensitive to the degree of myelination (Fujiyoshi et al., 2016), and used to study spinal cord maturation (Assaf et al., 2000) and degeneration (Farrell et al., 2010) in the rat. In addition, the EAP may be used to characterize age-related white matter (WM) demyelination in healthy populations (Fatima et al., 2013), differentiate lesions from normal appearing white matter and normal tissue in patients with multiple sclerosis (Assaf et al., 2002, 2005; Hori et al., 2014), and detect remyelination within the multiple sclerosis lesions (Fujiyoshi et al., 2016; Tanikawa et al., 2017). The EAP has also been used to map spinal cord diameter in an *ex vivo* rat (Ong and Wehrli, 2010; Ong et al., 2008) and *in vivo* human axon diameters (Hori et al., 2016; Kamiya et al., 2014). The various metrics derived from the EAP to characterize tissue microstructure properties include return-to-origin probability (or zero displacement probability) (Cohen and Assaf, 2002; Wu et al., 2008; Mitra et al., 1995; Descoteaux et al., 2011), displacement distance at half maximum (Cohen and Assaf, 2002), kurtosis (Fujiyoshi et al., 2016), mean-squared displacement (Cory, 1990; Cohen and Assaf, 2002; Wu et al., 2008), and fiber population dispersion (Assemlal et al., 2011), etc.

While model-based methods have several advantages, a model-free approach for recovering the EAP provided by DSI can be particularly valuable for studying brain regions where the tissue microstructure is not as well characterized as in white matter, such as in gray matter (GM), demyelinating lesion (Assaf et al., 2002, 2005; Fujiyoshi et al., 2016; Hori et al., 2014; Tanikawa et al., 2017), hemorrhagic lesion (Edlow et al., 2013, 2016), or a tumor (Taylor et al., 2017; Yamada et al., 2015). A model-free approach could also be valuable for diffusion measurements outside the brain (e.g. muscle (Wedeen et al., 2005; Taylor et al., 2015; Hoffman et al., 2018)) or even potentially for studying vasculature (Callaghan, 2011).

Unfortunately, the use of DSI's Fourier relationship between the q-space signal and the EAP (Eq. (1)) demands performing the Fast Fourier Transform (FFT) of q-space samples acquired on a 3D Cartesian grid (e.g. $11\times11\times11$ Cartesian grid with corners removed). The Cartesian sampling proposes several problems. Most importantly, the prescribed Cartesian q-space samples no longer locate on a strict Cartesian grid after the b-value and b-vector are corrected to account for gradient nonlinearity and subject motion (Leemans and Jones, 2009; Mesri et al., 2018; Guo et al., 2018), which decreases the accuracy of the FFT. Further, the Cartesian sampling is not optimal with many other analysis methods, such as diffusion tensor imaging (DTI) (Basser et al., 1994; Pierpaoli et al., 1996), neurite orientation dispersion and density imaging (Zhang et al., 2012) and the constrained spherical deconvolution (CSD) (Tournier et al., 2004, 2007; Jeurissen et al., 2014). In addition, the Cartesian diffusion data requires specialized data pre-processing. For example, the widely used "eddy" function (Andersson and Sotiropoulos, 2016) from the FMRIB Software Library (FSL) (Jenkinson et al., 2012; Smith et al., 2004) for eddy current correction and co-registration cannot process Cartesian data. The other problem with the Cartesian sampling is that the recovered EAP via the FFT also locates on a Cartesian grid, which is challenging to visualize and analyze (Vaillancourt et al., 2015). Last, the availability of Cartesian sampling protocols is limited on clinical MRI scanners.

Multi-shell q-space sampling has become the new standard for data acquisition. Some of the benefits of multi-shell sampling include the: (1) uniform angular resolution; (2) flexible sampling pattern and scan time (i.e. the number shells, and the b-value and the number of directions on each shell); (3) high compatibility with other processing and analysis methods; (4) capability to recover the EAP given sufficient sampling coverage, and (5) widely available protocols on clinical MRI scanners. Consequently, the multi-shell sampling scheme has been adopted by the MGH-USC (Setsompop et al., 2013; McNab et al., 2013; Fan et al., 2014) and WU-Minn-Ox (Sotiropoulos et al., 2013; Ugurbil et al., 2013; Van Essen et al., 2013) Human Connectome Project (HCP) to acquire gold standard diffusion data on a large population. Many widely used analysis methods which were originally proposed for single-shell diffusion data, such as q-ball imaging (QBI) (Aganj et al., 2010; Kamath et al., 2012; Tuch, 2004), CSD and Bayesian estimation of diffusion parameters obtained using sampling techniques for modeling crossing fibers (BEDPOSTX) (Behrens et al., 2003), are now also compatible with multi-shell data.

Most EAP reconstruction methods using multi-shell data are based on DSI's Fourier relationship, but impose a q-space signal model, relinquishing the benefits that arise due to DSI being model-free. For example, the diffusion orientation transform (DOT) method (Özarslan et al., 2006; Canales-Rodríguez et al., 2010a) assumes Gaussian diffusion. Alternatively, the multiple q-shell diffusion propagator imaging (mq-DPI) method (Descoteaux et al., 2009, 2011) models q-space signals as the solution of a Laplace equation in spherical coordinates. The Bessel Fourier orientation reconstruction (BFOR) (Hosseinbor et al., 2013) models q-space signals using the heat equation. The spherical polar Fourier imaging (SPFI) (Assemlal et al., 2009) method models q-space signals in terms of Gaussian-Laguerre polynomials. The mean apparent propagator (MAP)-MRI (Özarslan et al., 2013) method models q-space signals in terms of Hermite polynomials. For each approach, the accuracy and robustness to noise of the imposed model needs to be evaluated comprehensively for different microstructural configurations and q-space sampling schemes (e.g. maximum b-value).

Compared to the abundance of the model-based methods described above, there are very few model-free methods for reconstructing the EAP from multi-shell data. In hybrid diffusion imaging (HYDI), the multi-shell q-space samples are gridded to a Cartesian lattice (similar to k-space gridding (Beatty et al., 2005)) for a FFT-based DSI reconstruction (Wu and Alexander, 2007). The HYDI method has been used to directly compute EAP measures such as the zero displacement probability, mean-squared displacement and diffusion ODF but does not provide a complete solution of the EAP (Wu et al., 2008). The optimal way for gridding the q-space data has not been investigated. Further, the gridding process is also computationally expensive. Generalized q-sampling imaging (GQI) provides model-free diffusion ODF (Yeh et al., 2010; Tian et al., 2017a) and has been applied to multi-shell radial q-space samples (Baete et al., 2015; Baete and Boada, 2017). GQI, however, does not reconstruct the EAP.

In the current study, we developed a generalized DSI (GDSI) framework that is compatible with both Cartesian and non-Cartesian q-space

diffusion MRI data. GDSI recovers the EAP in a preferable arbitrary coordinate system using the Discrete Fourier Transform (DFT). Scalar metrics such as zero displacement probability and displacement distance at half maximum can be easily computed from GDSI's EAP and are shown useful to characterize the diffusion process in different tissue types. Using GDSI's matrix formalism, the contribution and combination of q-space signals to the diffusion ODF is elucidated. The fiber crossing angles estimated by model-free and model-based methods are depicted. GDSI is tested on multiple different types of multi-shell datasets including those from the HCP.

2. Theory

In DSI, the EAP $P(\boldsymbol{r})$ is recovered from the Fourier transform of the normalized q-space signal $S(\boldsymbol{q})$ (Callaghan et al., 1988; Callaghan, 1991, 1996; Mitra and Halperin, 1995) as:

$$P(\boldsymbol{r}) = \mathscr{F}(S(\boldsymbol{q})) = \iiint_{\boldsymbol{q}\in\mathbb{R}^3} S(\boldsymbol{q}) e^{-2\pi i \boldsymbol{q}\cdot\boldsymbol{r}} d\boldsymbol{q}. \tag{1}$$

$\mathscr{F}$ denotes the Fourier transform. $\boldsymbol{r}$ is the 3D spatial vector describing a spin displacement ($r\boldsymbol{u}$, with $r = |\boldsymbol{r}|$ the displacement distance and unit vector $\boldsymbol{u}$ the displacement direction). $\boldsymbol{q}$ is the gradient wave vector (or q-space points) describing the diffusion-encoding scheme ($q\boldsymbol{v}$, with $q = |\boldsymbol{q}|$ the encoding strength and unit vector $\boldsymbol{v}$ the encoding direction). q is proportional to the product of the strength and duration of a rectangle diffusion-encoding gradient, and proportional to the square root of b-value (Eq. (A2)).

As $S(\boldsymbol{q})$ is real and symmetric and $P(\boldsymbol{r})$ is real (Wedeen et al., 2005), the exponential function in Equation (1) can be reduced to a cosine function (Yeh et al., 2010; Paquette et al., 2016) as:

$$P(\boldsymbol{r}) = \iiint_{\boldsymbol{q}\in\mathbb{R}^3} S(\boldsymbol{q}) \cos(2\pi \boldsymbol{q}\cdot\boldsymbol{r}) d\boldsymbol{q}. \tag{2}$$

For a finite number (N) of measured q-space samples, the EAP is calculated as a linear weighted summation of all diffusion signals as:

$$P(\boldsymbol{r}) = \sum_{i=1}^{N} S(\boldsymbol{q}_i) \cos(2\pi \boldsymbol{q}_i\cdot\boldsymbol{r}) \Delta\boldsymbol{q}_i, \tag{3}$$

or in matrix form:

$$\underbrace{\begin{bmatrix} P(\boldsymbol{r}_1) \\ \vdots \\ P(\boldsymbol{r}_M) \end{bmatrix}}_{P} = \underbrace{\begin{bmatrix} \cos(2\pi\boldsymbol{q}_1\cdot\boldsymbol{r}_1) & \cdots & \cos(2\pi\boldsymbol{q}_N\cdot\boldsymbol{r}_1) \\ \vdots & \ddots & \vdots \\ \cos(2\pi\boldsymbol{q}_1\cdot\boldsymbol{r}_M) & \cdots & \cos(2\pi\boldsymbol{q}_N\cdot\boldsymbol{r}_M) \end{bmatrix}}_{F} \underbrace{\begin{bmatrix} \Delta\boldsymbol{q}_1 & & 0 \\ & \ddots & \\ 0 & & \Delta\boldsymbol{q}_N \end{bmatrix}}_{C} \underbrace{\begin{bmatrix} S(\boldsymbol{q}_1) \\ \vdots \\ S(\boldsymbol{q}_N) \end{bmatrix}}_{S}. \tag{4}$$

P is a column vector ($M\times1$) of recovered EAP values evaluated at spin displacements $\boldsymbol{r}_j$ ($1 \le j \le M$, $j\in\mathbb{Z}$). $\boldsymbol{r}_j$ can reside in an selected coordinate system, e.g. Cartesian or polar, to assist the visualization and analysis of the EAP. F is the DFT matrix ($M\times N$). C is the diagonal q-space sampling density non-uniformity correction matrix ($N\times N$). S is a column vector ($N\times1$) of the normalized attenuated echo signal measured at q-space location $\boldsymbol{q}_i$ ($1 \le i \le N$, $i\in\mathbb{Z}$).

Provided the gradient separation (Δ) and duration (δ) are kept constant, the spin dephasing term ($\Phi = 2\pi\boldsymbol{q}\boldsymbol{r}$) in each element of matrix F can be expressed using the commonly reported b-value (b) and b-vector ($\boldsymbol{v}$) of the diffusion pulse sequence following GQI's derivation (Yeh et al., 2010) (see Appendix A) as:

$$F = \begin{bmatrix} \cos(\sqrt{6D_{water}b_1}\,\boldsymbol{v}_1\cdot\lambda_1\boldsymbol{u}_1) & \cdots & \cos(\sqrt{6D_{water}b_N}\,\boldsymbol{v}_N\cdot\lambda_1\boldsymbol{u}_1) \\ \vdots & \ddots & \vdots \\ \cos(\sqrt{6D_{water}b_1}\,\boldsymbol{v}_1\cdot\lambda_M\boldsymbol{u}_M) & \cdots & \cos(\sqrt{6D_{water}b_N}\,\boldsymbol{v}_N\cdot\lambda_M\boldsymbol{u}_M) \end{bmatrix}. \tag{5}$$

D_{water} ($2.5\times10^{-3}\,\mathrm{mm^2/s}$) is the diffusion rate of free water at 37 °C. λ_j ($1 \le j \le M$, $j\in\mathbb{Z}$) is the scalar that relates an arbitrary displacement distance r_j and the mean displacement distance of free water (MDD_{water}). $MDD_{water} = \sqrt{6D_{water}(\Delta - \delta/3)}$ is calculated using Einstein's equation (Einstein, 1905) with effective diffusion time Δ-$\delta/3$ and an assumption of Gaussian diffusion. MDD_{water} is a constant number for all voxels, given the constant diffusion encoding timing Δ and δ in a diffusion pulse sequence, and represents the longest displacement a spin can transverse in a specific experiment. It is more intuitive to express an arbitrary distance r_j as a ratio of this upper bound compared to using actual numbers.

Each diagonal element $\Delta\boldsymbol{q}_i$ of C represents the q-space volume associated with each q-space samples $\boldsymbol{q}_i$ ($1 \le i \le N$, $i\in\mathbb{Z}$). The signal measured at a sparsely sampled q-space location associates with a large q-space volume and is therefore scaled up, and vice versa.

To summarize the EAP's angular structure, the diffusion ODF is calculated by a radial integration of the EAP weighted by the displacement distance (r) to the power of n, along multiple directions as:

$$O_{r_s,r_e,n}(\boldsymbol{w}) = \int_{r_s}^{r_e} P(r\boldsymbol{w}) r^n dr. \tag{6}$$

Unit vector $\boldsymbol{w}$ denotes the direction along which the diffusion ODF is being computed. r_s and r_e is the starting and ending displacement distance along $\boldsymbol{w}$ respectively for the radial integration. n is the power of displacement distance. When $n = 0$ (e.g. in QBI), the ODF represents the ensemble probability that spins displace along a certain direction. When $n = 2$ (e.g. in DSI), the ODF represents the mean squared displacement distance along a certain direction. A larger n results in a diffusion ODF with higher contribution from the EAP at longer displacement distance.

The diffusion ODF can be calculated using a direct and indirect approach from the EAP. For the indirect approach, the EAP is first recovered along radial lines in the directions that the ODF will be reconstructed (using Eqs. (4) and (5)) and then integrated. The EAP can be modified prior to ODF calculation, e.g. clipping the negative lobes of the ringing.

For the direct approach, the DFT and the radial integration are combined into a single step. The direct approach is advantageous for reducing computation and elucidating the relationship between q-space samples and the ODF, but does not allow modifying the EAP before the integration. Specifically, for a finite number of displacements with distances evenly spaced between r_s and r_e, ODF is calculated as a linear weighted summation of EAP values as:

$$O_{r_s,r_e,n}(\boldsymbol{w}) = \sum_{j=1}^{M} P(r_j\boldsymbol{w}) r_j^n \Delta r_j \left(r_s \le r_j \le r_e\right), \tag{7}$$

or in matrix form:

$$\underbrace{\begin{bmatrix} O_{r_s,r_e,n}(\boldsymbol{w}_1) \\ \vdots \\ O_{r_s,r_e,n}(\boldsymbol{w}_L) \end{bmatrix}}_{O_{r_s,r_e,n}} = \Delta r \underbrace{\begin{bmatrix} \left[r_1^n \cdots r_M^n\right] & \cdots & 0 \\ \vdots & \ddots & \vdots \\ 0 & \cdots & \left[r_1^n \cdots r_M^n\right] \end{bmatrix}}_{I_{r_s,r_e,n}} \underbrace{\begin{bmatrix} P(r_1\boldsymbol{w}_1) \\ \vdots \\ P(r_M\boldsymbol{w}_1) \\ \vdots \\ P(r_1\boldsymbol{w}_L) \\ \vdots \\ P(r_M\boldsymbol{w}_L) \end{bmatrix}}_{P}. \tag{8}$$

$O_{r_s,r_e,n}$ is a column vector ($L\times1$) of recovered ODF values evaluated along directions $\boldsymbol{w}_k$ ($1\le k\le L$, $k\in\mathbb{Z}$) for a given set of r_s, r_e and n. $\Delta r=(r_e-r_s)/(M-1)$ is a constant term accounting for the distance interval Δr_j for displacement r_j ($1\le j\le M$, $j\in\mathbb{Z}$, $r_s\le r_j\le r_e$, $r_1=r_s$, $r_M=r_e$). $I_{r_s,r_e,n}$ is the weighted summation matrix ($L\times ML$) of the radial integration of the EAP. P is a column vector ($ML\times1$) of the EAP values along directions $\boldsymbol{w}_k$ at displacement distances r_j.

Substituting Equations (4) and (5) into (8) provides a solution for the ODF directly from the q-space signals:

$$\underbrace{\begin{bmatrix} O_{\lambda_s,\lambda_e,n}(\boldsymbol{w}_1) \\ \vdots \\ O_{\lambda_s,\lambda_e,n}(\boldsymbol{w}_L) \end{bmatrix}}_{O_{\lambda_s,\lambda_e,n}} = \Delta r\cdot MDD_{water}^{n}\cdot \underbrace{\begin{bmatrix} \sum_{j=1}^{M}\cos\left(\sqrt{6D_{water}b_1}\,\boldsymbol{v}_1\cdot\lambda_j\boldsymbol{w}_1\right)\cdot\lambda_j^n & \cdots & \sum_{j=1}^{M}\cos\left(\sqrt{6D_{water}b_N}\,\boldsymbol{v}_N\cdot\lambda_j\boldsymbol{w}_1\right)\cdot\lambda_j^n \\ \vdots & \ddots & \vdots \\ \sum_{j=1}^{M}\cos\left(\sqrt{6D_{water}b_1}\,\boldsymbol{v}_1\cdot\lambda_j\boldsymbol{w}_L\right)\cdot\lambda_j^n & \cdots & \sum_{j=1}^{M}\cos\left(\sqrt{6D_{water}b_N}\,\boldsymbol{v}_N\cdot\lambda_j\boldsymbol{w}_L\right)\cdot\lambda_j^n \end{bmatrix}}_{R_{\lambda_s,\lambda_e,n}}$$

$$\underbrace{\begin{bmatrix} \Delta\boldsymbol{q}_1 & & 0 \\ & \ddots & \\ 0 & & \Delta\boldsymbol{q}_N \end{bmatrix}}_{C}\underbrace{\begin{bmatrix} S(\boldsymbol{q}_1) \\ \vdots \\ S(\boldsymbol{q}_N) \end{bmatrix}}_{S}, \tag{9}$$

where $\lambda_s\le\lambda_j\le\lambda_e$ ($1\le j\le M$, $j\in\mathbb{Z}$), $\lambda_1=\lambda_s=r_s/MDD_{water}$, $\lambda_M=\lambda_e=r_e/MDD_{water}$. If Δr and MDD_{water}^{n} are set to 1, this only affects the scaling the absolute values of the ODF and therefore there is no loss of angular information. $R_{\lambda_s,\lambda_e,n}$ is the reconstruction matrix ($L\times N$) of ODF values. An ODF value $O_{\lambda_s,\lambda_e,n}(\boldsymbol{w}_k)$ along a specific direction $\boldsymbol{w}_k$ is computed as a linear weighted summation of all sampling density corrected q-space signals, with linear weights determined by the kth row of $R_{\lambda_s,\lambda_e,n}(\boldsymbol{w}_k)$.

Equation (9) formulates the DSI ODF reconstruction as a linear system, which provides an intuitive perspective to understand the relationship between the q-space signal and the ODF. To visualize the contribution and combination of q-space samples to the ODF, the row of $R_{\lambda_s,\lambda_e,n}$ for computing the ODF value along the q_z-axis (Fig. 1 bottom to top) was calculated, with parameters $\lambda_s=0$, $\lambda_e=1$, and $n=0$ ($R_{0,1,0}(q_z)$ in Fig. 1a) or $n=2$ ($R_{0,1,2}(q_z)$ in Fig. 1b). $R_{0,1,0}(q_z)$ and $R_{0,1,2}(q_z)$ are displayed as 1D profile along the q_z-axis (Fig. 1a, c), 2D cross-section on the q_y-q_z plane (Fig. 1b, d), and 3D contour at single q(b)-values (Fig. 1e and f). The weights are rotationally symmetric about the q_z-axis (Fig. 1b, d, e, f), since the weight of a specific q-space sample is determined by the projection of its q-value to the q_z-axis (i.e. $\sqrt{b_i}\boldsymbol{v}_i\cdot\boldsymbol{w}_k$ in Eq. (9)). The 1D profile on the q_z-axis is a sinc function (Yeh et al., 2010; Tian et al., 2017b) (Fig. 1a), or resembles the shape of a sinc function (Fig. 1c).

The 3D contours of $R_{0,1,0}(q_z)$ for high b-values (e.g. Fig. 1e, $b\ge2{,}000$ s/mm^2) resemble thin discs (i.e., the weight for q-space points outside the q_x-q_y plane are close to zero), indicating that the ODF value along the q_z-axis is approximately the sum of signals on the equator of individual q(b)-values on the q_x-q_y plane, which is in agreement with QBI's use of the Funk-Radon transform. This approximation is more accurate (i.e. thinner disc) for higher b-values. In case of multiple q(b)-values, the ODF value along the q_z-axis can be approximated as the sum of signals on the entire q_x-q_y plane.

An ODF can be decomposed into component ODFs from individual q-

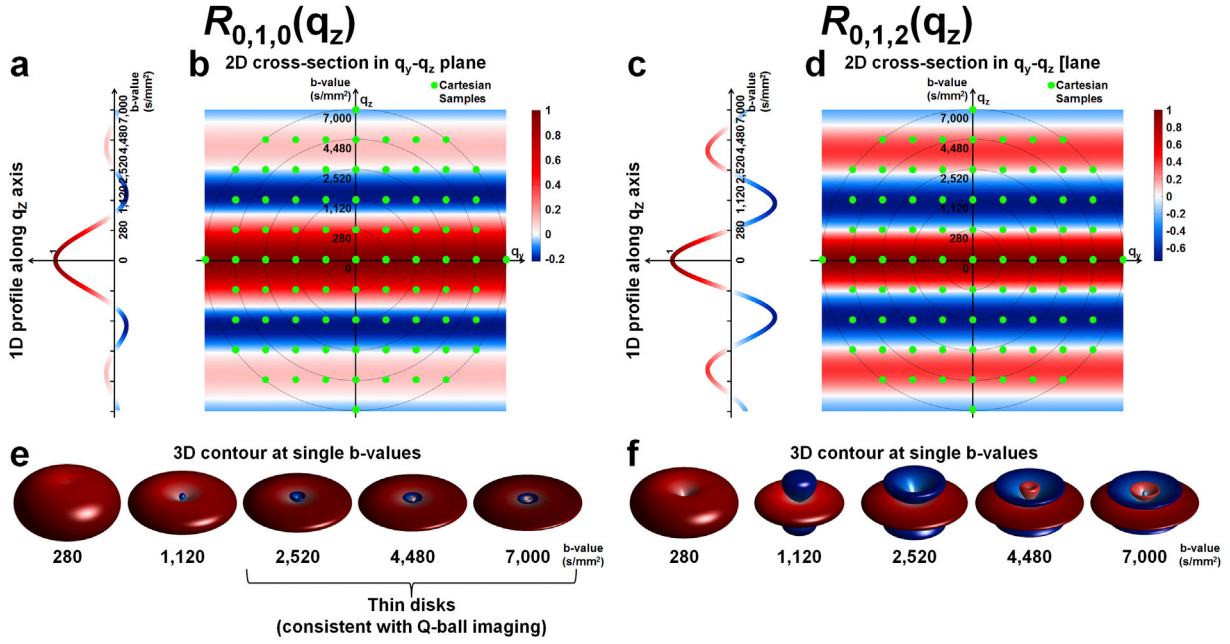

Fig. 1. The reconstruction matrix $R_{0,1,0}(q_z)$ and $R_{0,1,2}(q_z)$ for computing the orientation distribution function value along q_z-axis (bottom to top) with parameters $\lambda_s=0$, $\lambda_e=1$, $n=0$ (a, b, e) and $\lambda_s=0$, $\lambda_e=1$, $n=2$ (c, d, f). $R_{0,1,0}(q_z)$ and $R_{0,1,2}(q_z)$ are displayed as 1D profile along the q_z-axis (a, c), 2D cross-section on the q_y-q_z plane (b, d), and 3D contour at single q(b)-values (e, f). The green dots display the standard DSI-11 Cartesian q-space sampling locations with 7,000 s/mm^2 maximum b-value.

space samples by rewriting Equation (9) as:

$$O_{\lambda_s,\lambda_e,n} = \Delta r R_{\lambda_s,\lambda_e,n} C \underbrace{\left(S(\boldsymbol{q}_1)\begin{bmatrix}1\\0\\\vdots\\0\end{bmatrix} + S(\boldsymbol{q}_2)\begin{bmatrix}0\\1\\\vdots\\0\end{bmatrix} + \cdots + S(\boldsymbol{q}_N)\begin{bmatrix}0\\0\\\vdots\\1\end{bmatrix} \right)}_{S}$$
$$= \sum_{i=1}^{N} S(\boldsymbol{q}_i) O^{\boldsymbol{q}_i}_{\lambda_s,\lambda_e,n}. \quad (10)$$

$O^{\boldsymbol{q}_i}_{\lambda_s,\lambda_e,n}$ is the ith column of the matrix $R_{\lambda_s,\lambda_e,n}$, representing the impulse response ODF from a unit signal q-space sample located at point $\boldsymbol{q}_i$. The impulse response ODF from q-space samples located on the q_z-axis with different q(b)-values are displayed in Fig. 1e and f). $S(\boldsymbol{q}_i)O^{\boldsymbol{q}_i}_{\lambda_s,\lambda_e,n}$ is the component ODF from the q-space sample located at point $\boldsymbol{q}_i$.

Similarly, an ODF can also be decomposed into component ODFs from q-space samples with identical q(b)-values (i.e. individual shells).

3. Methods

3.1. Data simulation

Simulations were performed with a multi-tensor model using the "multi_tensor" function of the Diffusion Imaging in Python (DIPY) software (Garyfallidis et al., 2014) (http://nipy.org/dipy/). Each individual tensor had an axial diffusion rate of 1.6×10^{-3} mm^2/s and a radial diffusion rate of 0.2×10^{-3} mm^2/s. A noise-free three-fiber-crossing voxel (Fig. 2) was simulated for illustration purpose, with each fiber contributing 55%, 25% and 20% of the total signal, using the standard DSI 11×11×11 Cartesian sampling (hereafter referred as DSI-11) with 7,000 s/mm^2 maximum b-value.

3.2. Data acquisition

With Institutional Review Board (IRB) approval and written informed consent, data were acquired on a healthy subject using a clinical 3 Tesla MRI system (Discovery MR750, GE Healthcare, Milwaukee, Wisconsin) at Stanford. The scanner was equipped with a 32-channel radio frequency receive coil (Nova Medical, Wilmington, Massachusetts). A 2D single-refocused PGSE single-shot (SS) echo-planar-imaging (EPI) sequence was used to acquire multi-shell diffusion-weighted image (DWI) volumes of 30 contiguous axial slices covering the corpus callosum (CC). The data have: TE/TR = 95.7/2,000 ms, resolution = 2×2×2 mm^3, diffusion time (Δ) = 48.2 ms, gradient duration (δ) = 31.8 ms, 6 shells (including q-space origin, hereafter referred to as MSL-6, 33×b = 0, 103×b = 1,400 s/mm^2, 103×b = 2,800 s/mm^2, 103×b = 4,200 s/mm^2, 103×b = 5,600 s/mm^2, 103×b = 7,000 s/mm^2), ASSET parallel imaging factor R = 2. Two non-DWI (b = 0) volumes with reversed phase-encoding direction were acquired at the beginning of the scan. Non-DWI volumes were interleaved between every 16 DWI volumes.

3.3. Human Connectome Project data

Pre-processed whole-brain T_1-weighted and multi-shell diffusion data of subject 1010 from the MGH-USC HCP consortium and subject 100307 from the WU-Minn-Ox HCP consortium were downloaded for analysis (https://www.humanconnectome.org/). The diffusion data from both sites were acquired using 2D single-refocused PGSE SS EPI sequences. The MGH-USC diffusion data have: resolution = 1.5×1.5×1.5 mm^3, Δ = 21.8 ms, δ = 12.9 ms, 5 shells (MSL-5, 40×b = 0, 64×b = 1,000 s/mm^2, 64×b = 3,000 s/mm^2, 128×b = 5,000 s/mm^2, 256×b = 10,000 s/mm^2), maximum q-value (q_{max}) = 0.12 μm^{-1} (Fan et al., 2016). The WU-Minn-Ox diffusion data have: resolution = 1.25×1.25×1.25 mm^3, Δ = 43.1 ms, δ = 10.6 ms, 4 shells (MSL-4, 18×b = 0 s/mm^2, 90×b = 1,000 s/mm^2, 90×b = 2,000 s/mm^2, 90×b = 3,000 s/mm^2), q_{max} = 0.0438 μm^{-1} (Sotiropoulos et al., 2013). The MGH-USC T_1-weighted data were acquired with a multi-echo magnetization-prepared rapid acquisition gradient echo (ME-MPRAGE) sequence (van der Kouwe et al., 2008) at 1 mm isotropic resolution.

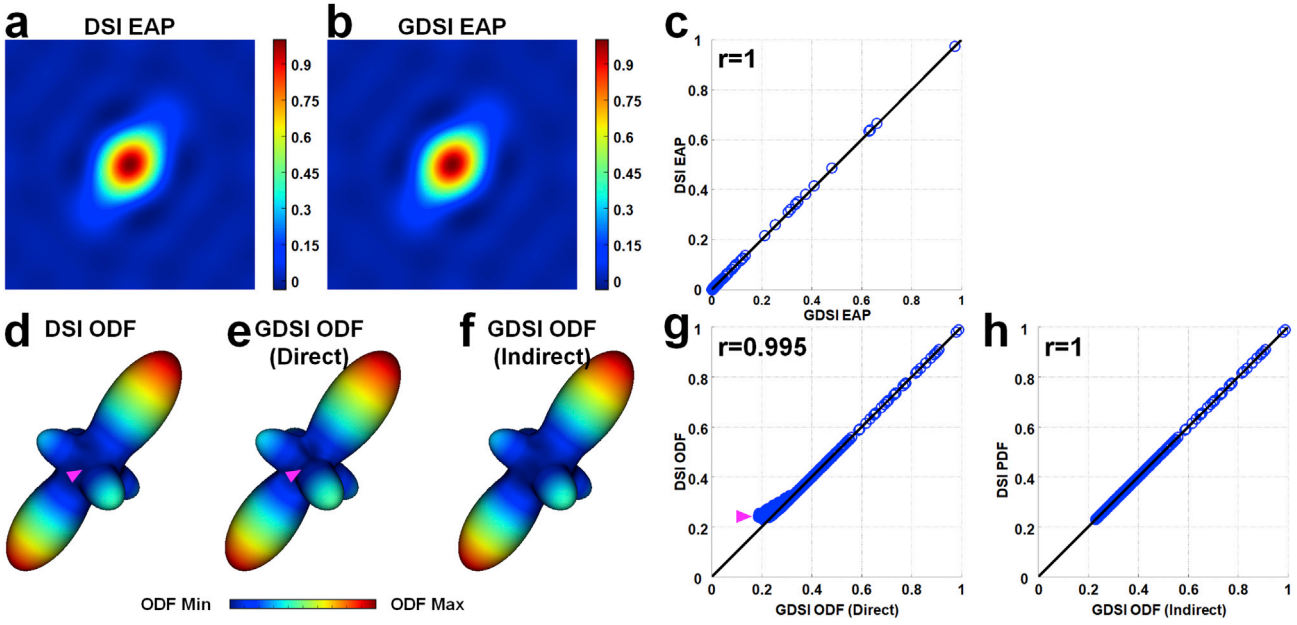

Fig. 2. Comparison of ensemble average propagator (EAP) (a, b) and diffusion orientation distribution function (ODF) (d-f) recovered from fast Fourier transform (FFT)-based diffusion spectrum imaging (DSI) (a, d) and proposed matrix formalism-based GDSI reconstruction (b, e, f) on a simulated noise-free three-fiber-crossing DSI-11 voxel. For both methods, the ODFs are reconstructed with $\lambda_s = 0$, $\lambda_e = 1$, $n = 2$. The ODF from the indirect QSI approach (f) was computed with the negative values of the EAP clipped to 0, the practice used in DSI reconstruction. The EAP and ODF are normalized by their maximum values. The scatter plots (c, g, h) depict 500 randomly selected values, with correlation from all values reported. The pink arrows highlight a region on ODF that demonstrates the effects of clipping negative values in EAP to 0 on the consequently reconstructed ODF.

3.4. Image processing

For the diffusion data acquired on-site at Stanford, the susceptibility-induced off-resonance field was estimated from the non-DWIs with opposite phase-encoding direction (Andersson et al., 2003) using FSL's "topup" function. The susceptibility-induced EPI distortion, eddy current distortion, field drift and bulk motion were corrected simultaneously using FSL's "eddy" function. The two non-DWI volumes with reversed phase-encoding direction were not used within subsequent analysis steps.

3.5. Regions of interest

For MGH-USC T_1-weighted data, cortical surface reconstruction and volumetric segmentation were performed using FreeSurfer software (Dale et al., 1999; Fischl and Dale, 2000) (https://surfer.nmr.mgh.harvard.edu/). The volumetric segmentation results (provided by aparc + aseg.mgz) were co-registered to the diffusion data using FreeSurfer's "bbregister" function with nearest neighbor interpolation. Binary masks of 14 regions of interest (ROIs) (i.e. ventricle, white matter (WM), CC, cerebellar WM, gray matter (GM), thalamus, accumbens, amygdala, caudate, putamen, pallidum, hippocampus, brainstem, and cerebellar GM), each containing both hemispheres, were created. The ventricle mask was created using FreeSurfer's "mri_binarize" function with the "ventricles" option selected. The CC mask was created by combining masks of five sub-regions of CC, i.e. the anterior, mid-anterior, central, mid-posterior and posterior parts (Fig. 8g). Only voxels with FA from DTI larger than 0.5 in the CC mask were included. Three ROIs covering parts of pre- and post-central gyrus, through the center of the thalamus and the pons of the brainstem (red boxes in Fig. 6b-d) were manually selected on axial slices based on FreeSurfer's volumetric segmentation.

For the HCP data from both consortiums, binary masks of the WM were resampled from FreeSurfer's volumetric segmentation and eroded by one voxel.

For each dataset, one ROI located in the centrum semiovale (CSO) region (Fig. 10), containing the intersection of three white matter fiber bundles (the CC, the corona radiata (CR), and the superior longitudinal fasciculus (SLF)), was manually selected based on DTI FA maps. The ROIs from each dataset all contain 8×10 voxels, but cover slightly different spatial extension due to the different spatial resolution of each dataset. A voxel with intra-voxel crossing fibers from each dataset (Fig. 10 magenta dashed boxes) was selected for demonstration (Figs. 5 and 9).

3.6. Q-space sampling density correction

Numerical computation based on 3D Voronoi diagram (Rasche et al., 1999) can be used for estimating the sampling density non-uniformity correction factor for various q-space sampling patterns. For multi-shell q-space samples, a simple geometry based approach was adopted (Fig. 4a), in a similar way that the correction factor is calculated for gridding the k-space data acquired with projection or radial trajectories (Pauly, 2005).

Specifically, contours (middle shells) (Fig. 4a colored circles) were generated half-way between each q-space sampling shell to delineate the radial extent associated with each q-space sample. For the outermost q-space sampling shell, the outer radial extent (Fig. 4a bold green circle) was set to be an equal distance from the q-space sample as the inner contour boundary.

For the sample located at the q-space origin (a single sample for the averaged $b = 0$ image), the correction factor is the volume of the central sphere. For DW samples located on each shell, the correction factor is the volume associated with the space between the inner and outer contours divided by the number of samples on the shell (assuming the q-space samples are uniformly distributed on each shell).

Mathematically, the correction factor V_{q_i} for a sample located on the ith shell with q-value q_i is:

$$V_{q_i} = \frac{\left(\frac{q_i+q_{i+1}}{2}\right)^3 - \left(\frac{q_i+q_{i-1}}{2}\right)^3}{N_{q_i} \cdot \left(\frac{q_2}{2}\right)^3}, \tag{11}$$

where $q_0 = q_1 = 0$, $q_{ns+1} = (3q_{ns}\text{-}q_{ns\text{-}1})/2$, $q_i < q_{i+1}$, $1 \le i \le ns$. q_1 and q_2 correspond to the $b = 0$ and smallest non-zero b-value. ns is the number of shells. N_{q_1} is the number of samples on a shell of q-value q_i. The volume of the central sphere $\left(\frac{q_2}{2}\right)^3$ is divided such that the correction factor V_{q_1} for the q-space sample at origin is equal to 1 and therefore the normalized non-DW signal (equal to the sum of EAP values) is still 1 after density correction. As the diffusion time is kept constant, the q-value in Equation (11) can be replaced by the square root of the corresponding b-value (Eq. (A3)).

3.7. DSI and GDSI reconstruction

The proposed GDSI (Eqs. (4), (5) and (9)) method was implemented in the framework of the DIPY software (available at https://github.com/qiyuantian/GDSI). For the simulated DSI-11 voxel, DSI reconstruction was performed using DIPY's "DiffusionSpectrumModel". The EAP was recovered on a Cartesian grid with a FOV of $2\times MDD_{\text{water}}$ along each dimension. The diffusion ODF was computed by integrating the EAP (negative values clipped to 0) from the center to the MDD_{water}. GDSI reconstruction was performed with identical parameters as DSI reconstruction to obtain the EAP and diffusion ODF (i.e. $\lambda_s = 0$, $\lambda_e = 1$, $n = 2$). Q-space sampling density correction was not used since q-space was uniformly sampled on a Cartesian grid. The GDSI ODF was computed using both the direct and indirect approach. For the direct approach, the impulse response ODF and the component ODF of each q-space sample were reconstructed. Component ODFs were computed for subsets of q-space signals with maximum b-values equal to: 0, 280 s/mm^2, 1,120 s/mm^2, 2,520 s/mm^2, 4,480 s/mm^2, and 7,000 s/mm^2. For the indirect approach, the negative values of the EAP were clipped to 0 (as performed in DSI) before calculating the ODF. The Pearson correlation of the EAP and ODF values from DSI and GDSI reconstruction was reported.

For crossing-fiber voxels from the CSO region from each dataset, EAP was reconstructed with and without q-space sampling density correction, on a Cartesian grid with a FOV of $2\times MDD_{\text{water}}$ along each dimension and along radial lines between 0 and MDD_{water}. The MDD_{water} for the Stanford, MGH-USC HCP and WU-Minn-Ox HCP data are 23.7 μm, 16.2 μm and 24.4 μm respectively.

For the MGH-USC HCP data, EAPs were recovered between 0 and MDD_{water} with q-space sampling density correction. Two scalar metrics were derived from the recovered EAPs:

(1) P_r: the probability at a specific displacement distance averaged across directions;
(2) r_α: the displacement distance at which the probability density decays to a fraction α of the maximum probability (i.e. zero displacement probability P_0) averaged across directions.

For the CC ROI, the displacement distance of the first zero crossing (r_0) was computed in the plane perpendicular to the primary eigenvector (V1) from DTI.

For each dataset, GDSI ODFs were reconstructed using the indirect approach with q-space sampling density and ringing removal (clipping the EAP values along each radial line beyond the first zero crossing to zero). The reconstruction parameters were $\lambda_s = 0$, $\lambda_e = 0.8$, $n = 2$ for the Stanford and MGH-USC HCP data, and $\lambda_s = 0$, $\lambda_e = 1$, $n = 2$ for the WU-Minn-Ox HCP data. The constant offset were removed. For voxels from the CSO ROI, the component ODFs from each single shell were also recovered.

The fiber orientations were delineated from the GDSI ODF using DIPY's "peaks_from_model" function. Specifically, the local maxima of a diffusion ODF with an amplitude larger than 5% of the global maximum

were first detected. If the angle between the two directions of local maxima was less than 15°, only the direction with the larger ODF amplitude was preserved. The directions were sorted according to their associated ODF amplitude. The first three directions were used as the primary, secondary and tertiary fiber orientations respectively.

3.8. DTI, BEDPOSTX, CSD and GQI reconstruction

For each dataset, the DTI model was fitted using FSL's "dtifit" function using only those shells with b-values less than 1,500 s/mm^2, to obtain the fractional anisotropy (FA) maps and V1.

The "ball and sticks" model was fitted using FSL's "bedpostx" function (3 sticks with a range of diffusivities). The estimated secondary and tertiary fiber orientations with fiber volume fraction lower than 5% were excluded.

Multi-shell multi-tissue CSD was performed using the MRTrix3 software (http://www.mrtrix.org/). The data were corrected for the B1 field inhomogeneity using MRTrix3's "dwibiascorrect" function. For each dataset, the segmentation of five tissue types (e.g. GM, WM) was first derived from the T_1-weighted data using MRTrix3's "5ttgen" function with the "fsl" option. The response functions were calibrated using MRTrix3's "dwi2response" function with the "msmt_5tt" option on brain voxels excluding the cerebellum. The fiber ODFs were then computed using MRTrix3's "dwi2fod" function. Three peaks for each fiber ODF were delineated using MRTrix3's "sh2peaks" function, without requirements on the peak amplitude. Within each voxel, the secondary and tertiary peaks were only preserved if their peak amplitudes were larger than 5% of the amplitude of the primary peak.

GQI reconstruction was performed using the "GeneralizedQSamplingModel" function from DIPY software. The reconstruction parameters were $\lambda_s = 0$, $\lambda_e = 0.8$, $n = 2$ for the Stanford and MGH-USC HCP data, and $\lambda_s = 0$, $\lambda_e = 1$, $n = 2$ for the WU-Minn-Ox HCP data, same as those used in GDSI. The fiber orientations were delineated from the GQI ODF using DIPY's "peaks_from_model" function in the same way as that used in GDSI.

3.9. Statistical analysis

For the MGH-USC HCP data, the mean and standard deviation of P_r and r_α within the 14 FreeSurfer ROIs were reported. The Pearson correlation of the T_1-weighted and P_0 values of brain voxels was reported. The mean and standard deviation of r_0 perpendicular to DTI V1 within the five FreeSurfer CC sub-regions were reported.

For the HCP data, the crossing angle in WM voxels between the primary and secondary fibers, the primary and tertiary fibers, and the secondary and tertiary fibers estimated using BEDPOSTX, CSD and GDSI were computed. The angle between two directions ($\boldsymbol{v}_1$, $\boldsymbol{v}_2$) was computed as $\cos^{-1}(|\boldsymbol{v}_1 \cdot \boldsymbol{v}_2|)$, ranging between ([0, 90°]).

4. Results

Our proposed DFT-based GDSI is equivalent to FFT-based DSI reconstruction. The EAPs (Fig. 2a and b) and diffusion ODFs (Fig. 2d–f) recovered from the simulated DSI-11 voxel using the two methods are qualitatively similar and quantitatively highly correlated (correlation larger than 0.995). The amplitudes along some directions on GDSI ODF (Fig. 2d, e, g pink arrows) computed using the direct approach are lower than those on DSI ODF, because the negative EAP values were not clipped to 0 in the direct approach.

GDSI's linear system formalism of the diffusion ODF reconstruction elucidates the contribution of q-space signals to a diffusion ODF. The diffusion ODF (reconstructed using the direct approach) from the simulated DSI-11 voxel (Fig. 3d) is a summation of 515 component ODFs (Fig. 3c, $S(\boldsymbol{q}_i)O^{\boldsymbol{q}_i}_{\lambda_s,\lambda_e,n}$ in Eq. (10)). Each component ODF is a multiplication

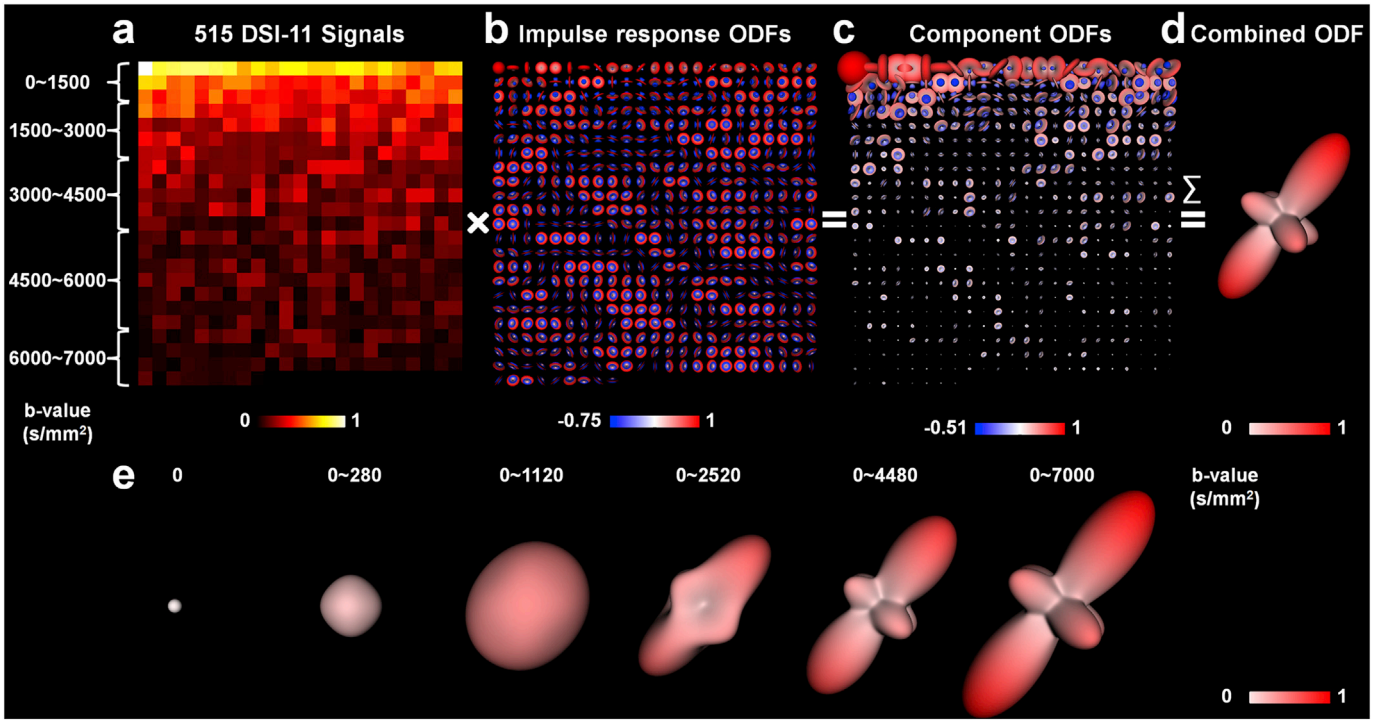

Fig. 3. Decomposition of the diffusion orientation distribution function (ODF) from the simulated noise-free three-fiber-crossing voxel (d) acquired using a standard diffusion spectrum imaging acquisition with 11×11×11 Cartesian grid and 7,000 s/mm^2 maximum b-value into component ODFs (c) from the 515 q-space signals (a), and component ODFs (e) from q-space signals with different maximum b-values (the six b-values along the left-right axis, i.e. 0, 280 s/mm^2, 1,120 s/mm^2, 2,520 s/mm^2, 4,480 s/mm^2, 7,000 s/mm^2). The q-space signals in (a) are arranged from low to high b-value in a 2D matrix (left to right, top to bottom). Each component ODF in (c) is the impulse response ODF (b) weighted by the diffusion signal intensity measured at the correspondent q-space location. The size of the impulse response ODF (b), component ODF (c, e) is proportional to the ODF value.

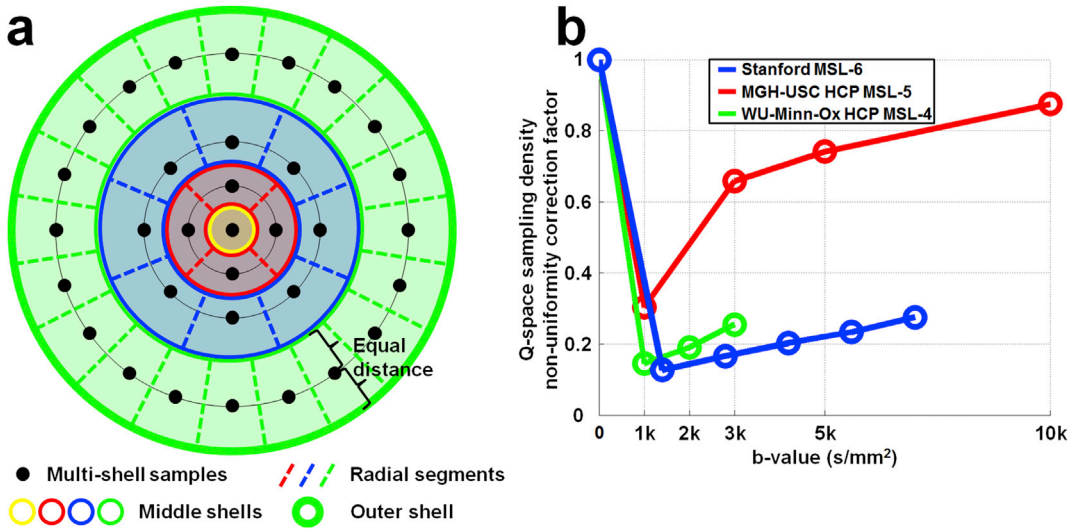

Fig. 4. A 2D illustration of the proposed geometrical approach to estimate the q-space sampling density correction factor, i.e. the volume associated with each q-space sample, assuming q-space samples are uniformly distributed on each shell (a), and the estimated results at each shell for the Stanford (b, blue curve), MGH-USC HCP (b, red curve) and WU-Minn-Ox HCP data (b, green curve). Four shells are depicted (including the origin) for illustration purpose. Note in (b) the x-axis is specified in b-value, which is square of the corresponding q-value.

of the signal intensity (Fig. 3a, arranged from low to high q(b)-value, in the left to right, top to bottom order) and the corresponding impulse response ODF (Fig. 3b, a column of $R_{\lambda_s,\lambda_e,n}$ in Eq. (9)) at a specific q-space sampling location. As the q(b)-value increases, the angular variation (high frequency information) of the impulse response ODF and component ODF increases, while the contribution (size) of the component ODFs to the combined ODF decreases. The combined diffusion ODF becomes sharper as more signals from high q(b)-values are included (Fig. 3e). Notably, the impulse response ODF and component ODF have both positive and negative values, while their summation is guaranteed to produce non-negative diffusion ODF.

Figure 4b displays the estimated q-space sampling density non-uniformity correction factors at each shell for the Stanford, MGH-USC HCP and WU-Minn-Ox HCP data using the proposed geometric method (Fig. 4a). For all three datasets, the sampling density correction factors for the $q(b)=0$ sample (a single sample for the averaged $b=0$ images) are relatively high, which scales up the non-DW signal and translates into an appropriate constant term in the EAP.

The correction factors for non-zero b-values are monotonically increasing, indicating that the signals from high q(b)-values are insufficiently sampled compared to low q(b)-values. The ratios between the correction factors of the lowest and the highest non-zero q-values are: 2.17, 2.89 and 1.76 for the Stanford, MGH-USC HCP and WU-Minn-Ox HCP data respectively. This means that the sampling density correction operation only moderately scales the signals from high q(b)-values while does not over-emphasize the noise in the low SNR measurements at high q(b)-values. For the MGH-USC HCP data, the slope of the correction factors for non-zero b-values decreases as the b-value increases (Fig. 4b red curve). This is because the MGH-USC HCP protocol partially compensated for the decreased sampling density at high b-values by doubling the number of samples as b-value increases from 3,000 s/mm^2 to 5,000 s/mm^2, as well from 5,000 s/mm^2 to 10,000 s/mm^2.

Figure 5 demonstrates the effects of q-space sampling density correction on the EAP. For the crossing-fiber voxels (from CSO region, Fig. 10 magenta dashed boxes), the 2D coronal cross sections through the center of the 3D EAP (Fig. 5a, b, d, e, g, h), the 1D profiles along left-right (Fig. 5c, f, i red curves), superior-inferior (Fig. 5c, f, i blue curves) and anterior-posterior (Fig. 5c, f, i green curves) directions from the EAP center, and the 3D contours (Fig. 5j, negative values clipped to 0) at different displacement distances are displayed. The EAP becomes sharper after the sampling density correction (comparing Fig. 5j rows i, iii, v with rows ii, iv and vi at displacement distance longer than 0.2 of the MDD_{water}) because the correction scales up high q(b)-value signals. The Gibbs ringing present in the EAP, however, becomes more severe (Fig. 5 pink arrows and dashed circles). The increased intensity of the Gibbs ringing after sampling density correction has the benefit of making the ringing easier to identify (comparing Fig. 5f solid and dashed lines), which assists operations to mitigate the effects of ringing, such as clipping the EAP values beyond the first zero-crossing to 0 before computing metrics and ODF from the EAP. Without sampling density correction, the ringing is harder to identify (e.g. Fig. 5f solid lines) and obscures the shape of EAP (e.g. Fig. 5j, rows iii, displacement distance larger than $0.4\times MDD_{\text{water}}$).

Due to the different $q_{\max}$ values for the Stanford, MGH-USC HCP and WU-Minn-Ox HCP datasets, the extents of the recovered EAP are different, i.e. about 2/3 (Fig. 5a and b), 1/2 (Fig. 5d and e) and 1 of MDD_{water} (Fig. 5g and h) respectively. Therefore, the displacement distance at which the 3D EAP contour is the sharpest is different, i.e. $0.6\times MDD_{\text{water}}=14.2$ μm, $0.5\times MDD_{\text{water}}=8.1$ μm, and $1\times MDD_{\text{water}}=24.4$ μm, for the Stanford (Fig. 5j, row ii), MGH-USC HCP (Fig. 5j, row iv) and WU-Minn-Ox HCP data (Fig. 5j, row vi).

Additional EAPs from brain regions where the tissue microstructure is more complex compared to the WM were recovered with q-space sampling density correction. These EAPs were reconstructed in the polar coordinates. For the MGH-USC HCP data, EAPs at 8 μm in ROIs that contain parts of pre- and post-central gyrus, thalamus and brainstem are displayed in Figure 6 (EAPs at 0-10 μm with 0.2 μm step are shown in supplementary videos). These EAPs present the diffusion patterns and map the complicated microstructure without imposing any model on the signal. In the post-central gyrus, for example, the water molecules have a high probability to diffuse in the direction radial to the cortical surface. Interestingly, a portion of the water molecules also tend to diffuse in the direction parallel to the cortical surface, resulting in crossing EAP orientations (Fig. 6b magenta dashed boxes). The sharp EAP contours also reveal multiple directional vectors of water diffusion in different thalamic nuclei and within the basis pontis in the brainstem.

Supplementary video related to this article can be found at https://doi.org/10.1016/j.neuroimage.2019.01.038

Figures 7 and 8 demonstrate two examples of metrics, i.e. P_r (Fig. 7) and r_α (Fig. 8) that can be derived from the recovered EAP. P_r represents the mean probability of a water molecule within a voxel displacing to a specific distance within the diffusion time used in the pulse sequence.

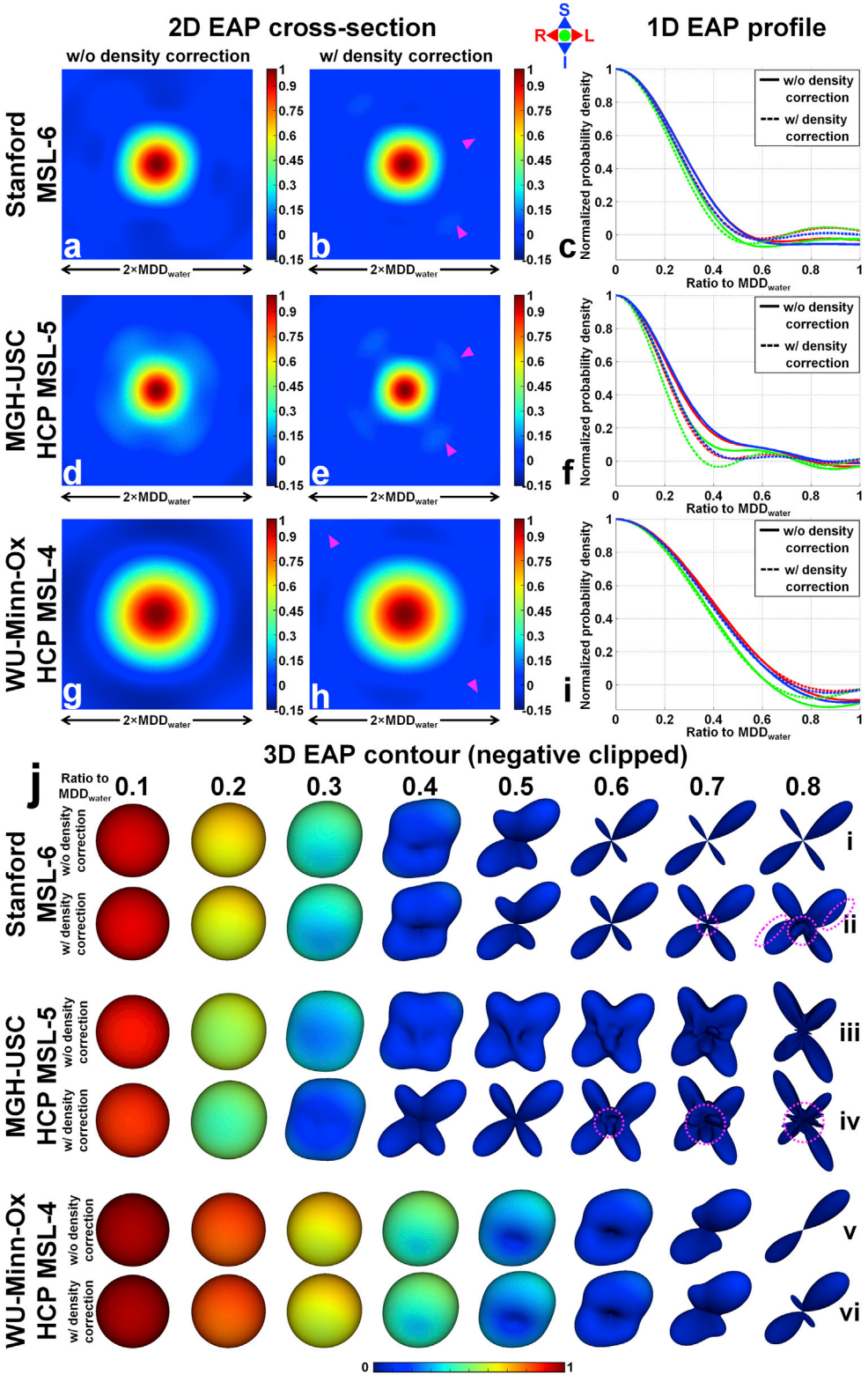

Fig. 5. Reconstructed spin displacement ensemble average propagator (EAP) with (b, e, h, dashed lines in c, f, i, and rows ii, iv, vi in j) and without (a, d, g, solid lines in c, f, i, and rows i, iii, v in j) q-space sampling density correction of crossing-fiber voxels (Fig. 10 magenta dashed boxes) from the Stanford (a-c, row i and ii in j), MGH-USC HCP (d-f, rows iii and iv in j) and WU-Minn-Ox HCP data (g-i, rows v and vi in j). The 2D coronal cross sections through the center of the 3D EAP (a, b, d, e, g, h), the 1D profiles along left-right (L-R, red lines in c, f, i), superior-inferior (S-I, blue lines in c, f, i) and anterior-posterior (A-P, green lines in c, f, i) directions from the EAP center, and the 3D contours (j, negative values clipped to 0) at different displacement distances are displayed. The mean displacement distance of free water (MDD_{water}) given the experimental timing is 23.7 μm, 16.2 μm, and 24.4 μm for the Stanford, MGH-USC HCP and WU-Minn-Ox HCP data respectively. The EAPs are normalized by their maximum values (i.e. the value at the EAP center). The pink arrows and dashed circles highlight the positive side lobes of the Gibbs ringing.

The mean P_r curve averaged from all WM voxels (Fig. 7f red, blue) is narrower than the mean P_r curves for the GM (Fig. 7f green) and cerebrospinal fluid (CSF) in the ventricle (Fig. 7f black) due to the more constrained water diffusion within the tightly packed axon bundles. At different displacement distances, P_r provides a new type of image contrast based on the diffusion property of the tissue (Fig. 7 b-e). At zero displacement distance, the P_0 map (Fig. 7b) resembles a T_1-weighted image (Fig. 7h, correlation equal to 0.58). Since the probability of water molecules in the WM and GM displacing to ~5.2 μm is similar (Fig. 7f pink arrow), the contrast between WM and GM is diminished in the $P_{5.2\mu m}$ map (Fig. 7c). For a displacement distance slightly longer than 5.2 μm, the P_r for the GM becomes larger than the P_r for the WM. Therefore, the GM is much brighter than the WM in the $P_{7\mu m}$ map, creating a strong GM-WM contrast. The CSF is the brightest in the $P_{15\mu m}$

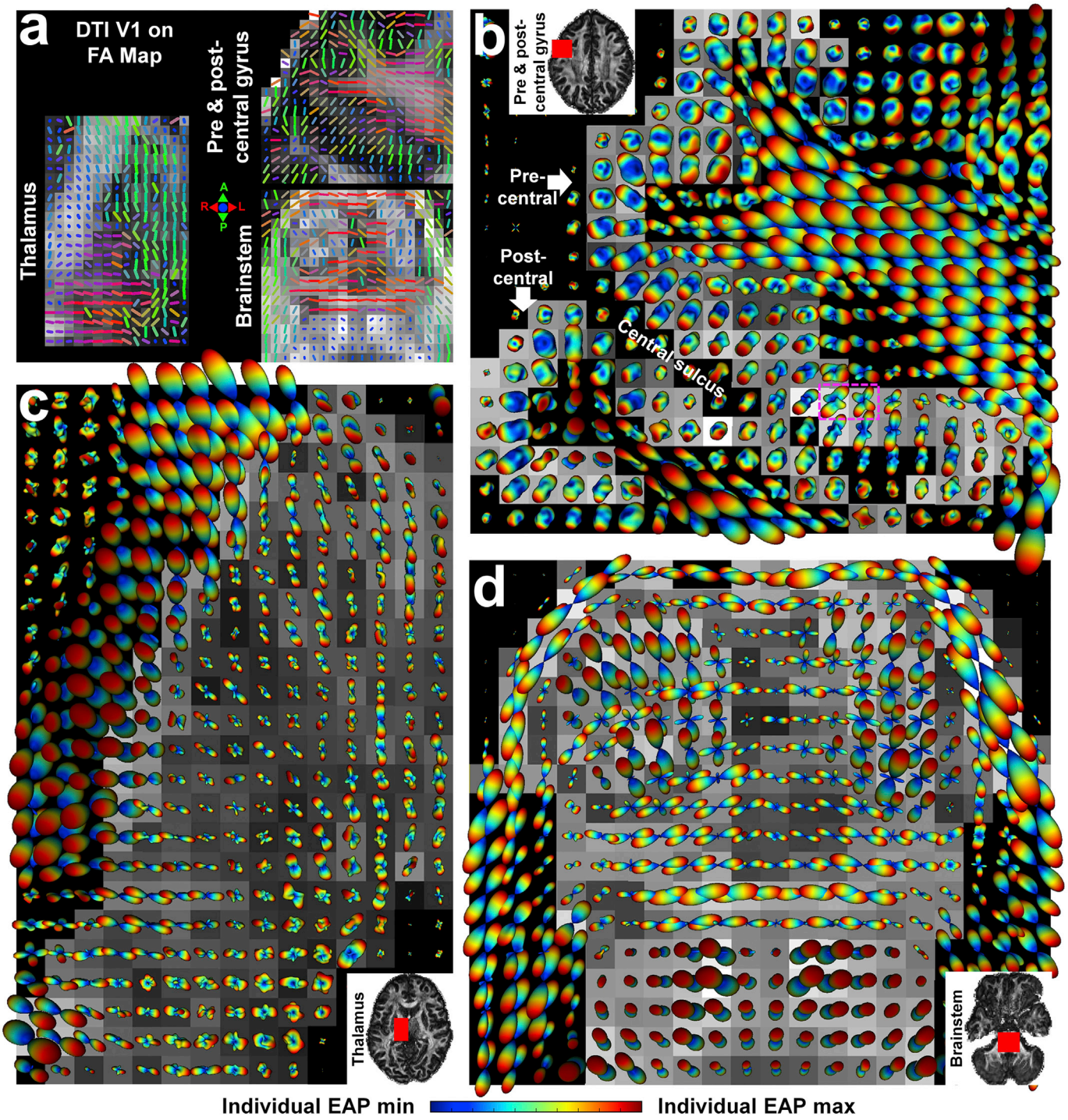

Fig. 6. Spin displacement ensemble average propagators (EAPs) recovered at 8 μm (with q-space sampling density correction) from the pre- and post-central gyrus, thalamus and brainstem regions of interest (ROIs, red rectangles in the inset images in b-d) from the MGH-USC HCP data overlaid on axial slices of fractional anisotropy (FA) maps (windowed between [0, 1]) from diffusion tensor imaging (DTI) (b–d). The nearby voxels outside the gray matter, thalamus and brainstem within the ROIs are on top of black background. The FA and the primary eigenvectors (V1) from DTI of the three ROIs are displayed in (a). DTI V1 is color coded based on orientation (red: left-right, green: anterior-posterior, blue: superior-inferior).

map since only water molecules with very fast diffusion rate can diffuse to such a long distance.

The r_α index measures the displacement distance that the mean probability decays to α of the maximum probability (i.e. P_0), and hence indicates the overall level of restriction within a voxel. As expected, WM appears darker than the GM and CSF in the r_α maps (Fig. 8a-f), revealing the increased degree of restricted diffusion within WM.

The r_0 index denotes the longest displacement distance that the water molecules can diffuse. Within the CC, r_0 in the direction perpendicular to the DTI V1 is different in different sub-regions (Fig. 8g and h). Specifically, the r_0 is larger in the body of the CC (Fig. 8g green, 5.65 ± 0.09 μm) compared to the anterior (Fig. 8g red, 5.55 ± 0.15 μm) and posterior part of the CC (Fig. 8g blue, 5.4 ± 0.15 μm). This corresponds well to histological studies in the literature that show that larger axon diameters are only found in the body of the CC and not in the genu and splenium of the CC (Aboitiz et al., 1992).

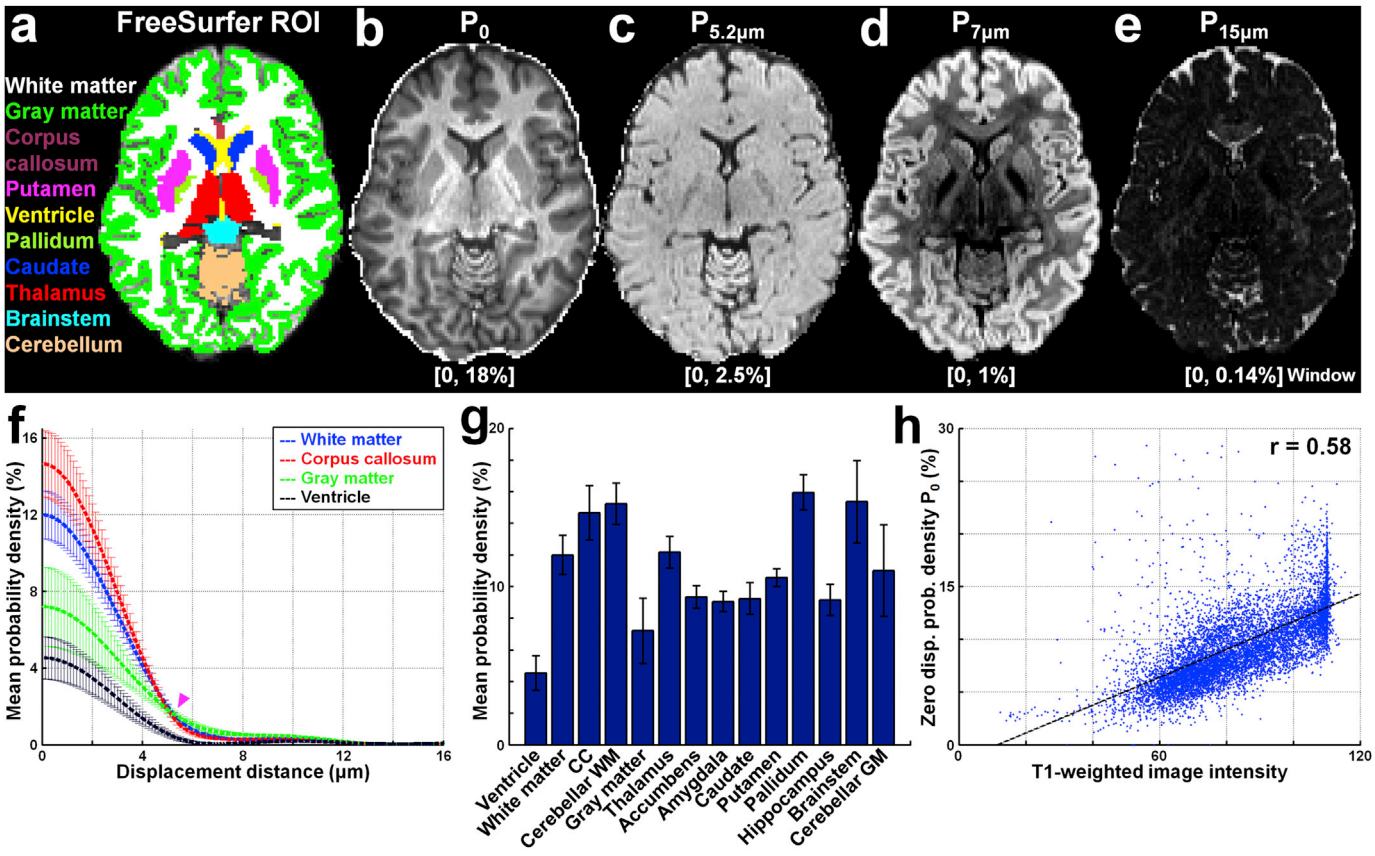

Fig. 7. Maps of the mean probability at 0 (b), 5.2 μm (c), 7 μm (d) and 15 μm (e) displacement distance on a representative axial slice, and the mean and standard deviation of the mean probability (f, g) within 14 FreeSurfer regions of interest (ROIs) (a, listed along the x-axis in g) from the MGH-USC HCP data. The scatter plot of the zero displacement probability versus the T_1-weighted image intensity in the whole brain is showed with the correlation value (h).

The effects of q-space sampling density correction on the ODF are demonstrated in Fig. 9. The component ODFs from each shell (Fig. 9 columns 1–6) and the combined ODF (Fig. 9 columns 7–8) reconstructed with (Fig. 9, rows ii, iv, vi) and without (Fig. 9, rows i, iii, v) sampling density correction for the Stanford (Fig. 9 rows i, ii), MGH-USC HCP (Fig. 9 rows iii, iv), and WU-Minn-Ox HCP data (Fig. 9 rows v, vi) are shown. The sampling density correction scales up the signals from high q(b)-value signals (weights determined in Fig. 4b) such that the component ODFs from high q(b)-value shell have higher contribution (larger size, the size of the component ODF from $b = 1000\ \mathrm{s/mm^2}$ were kept the same with and without the correction) to the combined ODF. Therefore, the combined ODF becomes sharper (comparing Fig. 9, rows i, iii, v with rows ii, iv, vi, column 7), with strengthened ringing obscuring the shape of the ODF and/or leading to "bumps" in the ODF (Fig. 9 green arrows) that might cause erroneous orientations to be used in the tractography. Using the indirect approach with ringing removal (clipping EAP values beyond the first zero crossing to 0), the ODF becomes much cleaner as well as sharper (comparing Fig. 9 columns 7 and 8).

Figure 10 displays the ODF and fiber orientations estimated using both model-based and model-free methods in the crossing fiber ROI from the CSO region. The GDSI ODFs are sharper compared to the GQI ODFs because the sampling density correction increases the contribution from the high q(b)-value signals that contain high frequency information in GDSI. Therefore, intra-voxel crossing fibers appear better delineated in GDSI compared to GQI (more blue and green sticks in Fig. 10b, rows 1, 3, 4, column iv than in column iii). For the model-free methods, detection of crossing fibers appears to be strongly dependent on the maximum b-value. Both GQI and GDSI identify more secondary and tertiary fibers in the MGH-USC HCP data with a maximum b-value of $10{,}000\ \mathrm{s/mm^2}$ compared to the WU-Minn-Ox HCP data with a maximum b-value of $3{,}000\ \mathrm{s/mm^2}$. The model-based methods overall identify more secondary and tertiary fibers compared to the model-free methods (more blue and green sticks in Fig. 10b, rows 1, 3, 4, columns i and ii, than in columns iii and iv, and supplementary simulation study).

The fiber crossing angles estimated by the model-based (BEDPOSTX and CSD) and model-free (GDSI) methods follow distinct distributions as depicted in Supplementary Figure 1 and Figure 11. The BEDPOSTX, CSD and GDSI method identifies a secondary fiber in 91%, 84% and 59% and a tertiary of fiber in 63%, 47% and 19% of all WM voxels in the MGH-USC HCP data, and identifies a secondary fiber in 95%, 78% and 9% and a tertiary of fiber in 70%, 26% and 0.7% of all WM voxels in the WU-Minn-Ox HCP data. For BEDPOSTX and CSD, the fiber crossing angle histograms show a peak ~60°, with an exception for the crossing angle between the primary and secondary fibers from the MGH-USC data (Fig. 11a, red curve, histogram peak shifted to ~30°). The fiber crossing angle histograms from CSD also have a preference for ~90°. For GDSI, the fiber crossing angle distribution resembles a half Gaussian curve centered at 90°.

5. Discussion

Here we present a generalized DSI framework to recover the model-free EAP from non-Cartesian diffusion data. Unlike conventional DSI, GDSI does not require Cartesian q-space sampling and FFT-based reconstruction. GDSI computes the EAP by multiplying the sampling non-uniformity corrected q-space samples with a DFT matrix, and is therefore flexible with the coordinate systems of both the q-space signals and the EAP. We demonstrate various metrics, such as the zero displacement probability, mean probability at a specific displacement distance, and the mean displacement distance at a fraction of the

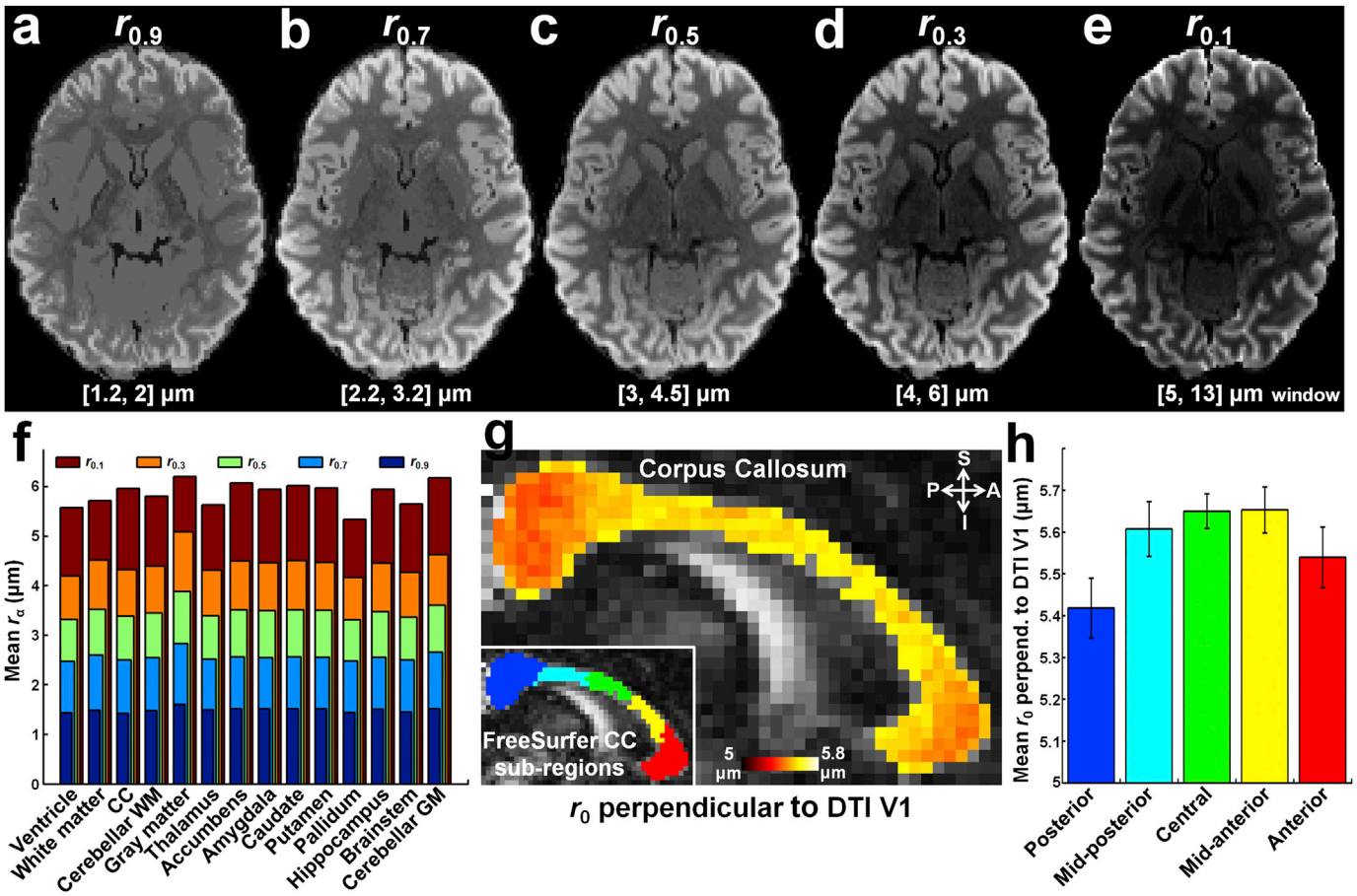

Fig. 8. Maps of the displacement distance at 0.9 (a), 0.7 (b), 0.5 (c), 0.3 (d), and 0.1 (e) of the zero displacement probability (P_0) on a representative axial slice, and their mean within 14 FreeSurfer region of interests (ROIs) (Fig. 7a, listed along the x-axis in f) from the MGH-USC HCP data. The map of the displacement distance at 0 probability (r_0, distance at first zero crossing) perpendicular to the primary eigenvector (V1) from diffusion tensor imaging (DTI) in the corpus callosum (CC) is displayed on fractional anisotropy (FA) map (windowed between [0, 1]) from DTI on a representative sagittal slice. The mean and standard deviation of r_0 within the five sub-regions of the CC (the anterior (red in g inset), mid-anterior (yellow in g inset), central (green in g inset), mid-posterior (cyan in g inset) and posterior (blue in g inset)) are reported in (h). Only voxels with FA larger than 0.5 within the FreeSurfer CC ROI are included.

maximum probability, can be derived from multi-shell diffusion data using our method to characterize tissue microstructure. Using the GDSI framework, we also elucidate the contribution and combination of q-space signals to the diffusion ODF by formulating the reconstruction as a linear system, and compute the model-free diffusion ODF from the multi-shell diffusion data.

The model-free EAP from GDSI is equivalent to the raw diffusion data, but provides a more intuitive representation in the Fourier domain, which more directly relates to the underlying diffusion patterns. For example, the shape of the EAP can reflect the restriction and non-Gaussianity of the diffusion process, which is useful for differentiating different tissue types (Fig. 7) and abnormal tissues. The size of the EAP (i.e. the width at the first zero-crossing) measures the longest displacement distance a water molecule can transverse during the diffusion time, which might reflect the trend of axon/nerve diameter (Fig. 8). This information provided by the EAP may be useful for microstructural imaging. Since the EAP also provides the ODF (EAP's angular summarization) for tractography purpose, the EAP potentially enables a way to integrate the microstructural imaging and diffusion tractography for characterizing microstructural properties associated with specific white matter fiber bundles (Huber et al., 2018; Yeatman et al., 2012, 2018).

The displacement distance associated with the GDSI EAP is different from the ground truth for two reasons. First, the narrow pulse assumption ($\delta \ll \Delta$), a condition of the Fourier relationship between the q-space signals and the EAP, cannot be met in practice. Therefore, the EAP describes the displacement of a spin from the mean position during the first pulsed gradient to the mean position during the second pulsed gradient. Consequently, the displacement distance is underestimated (Wedeen et al., 2005; Mitra and Halperin, 1995). Second, truncating the q-space before the signal decays to zero contaminates the EAP by convolving the true EAP with a point spread function (PSF) after the Fourier transform. The main lobe of the PSF blurs the EAP. The displacement distance is therefore overestimated (Tian et al., 2016). Therefore, any interpretation of displacement distance metrics derived from the EAP, such as r_α, should account for these approximations.

Fortunately, many approaches now exist to reduce the influence of these two issues on the EAP. For example, the stronger gradient strength provided by the HCP scanners (up to 300 mT/m from MGH-USC, and up to 80 mT/m from WU-Minn-Ox) achieves higher maximum b-values with shorter gradient durations, which not only brings the PGSE experiments closer to the narrow pulse approximation but also helps to mitigate the effects of q-space truncation. Alternatively, q-space truncation effects can be mitigated by deconvolving the EAP with the PSF associated with a specific q-space truncation (Canales-Rodríguez et al., 2010b) and reducing the noise floor for diffusion signal at high b-values using the real part rather than the magnitude of the signal (Eichner et al., 2015).

Our proposed EAP reconstruction method relies on solving the Fourier transform using a matrix formalism, i.e. multiplying the q-space signals with a DFT matrix. This approach allows performing the Fourier transform on signals acquired with any q-space sampling pattern, such as multi-shell, and provides a more general form of DSI. Therefore, the proposed GDSI method enables a more direct way to compare the DSI

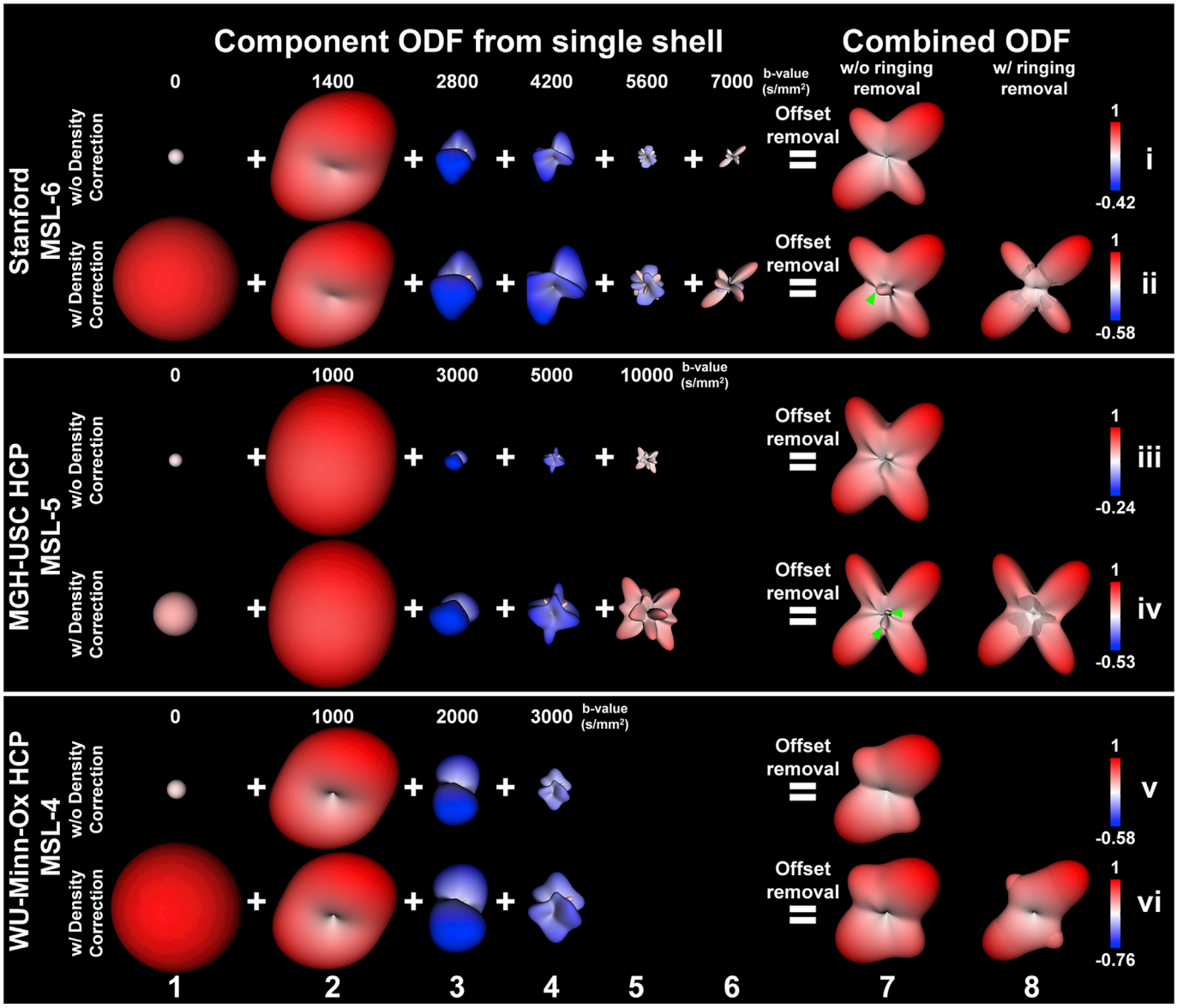

Fig. 9. Component orientation distribution functions (ODFs) from single shell (columns 1–6) and combined ODF (columns 7, 8) reconstructed with (rows ii, iv, vi) and without (rows i, iii, v) q-space sampling density correction, with (column 8) and without (column 7) ensemble average propagator (EAP) ringing removal from the Stanford (rows i, ii), MGH-USC HCP (rows iii, iv) and WU-Minn-Ox HCP data (rows v, vi). The size of the component ODF is proportional to their value. The size of the component ODF from the $b = 1{,}000\ \mathrm{s/mm^2}$ shell is kept the same with and without q-space sampling density correction. The combined ODF is normalized by their maximum.

based approach with many other model-based methods, such as CSD, on the same multi-shell data, without the confound of the different datasets required for different methods (e.g. Cartesian sampling data for DSI versus multi-shell sampling data for other model-based methods). The crossing fiber detection of model-free methods was found strongly dependent on the maximum b-value and less sensitive compared to the model-based methods (Figs. 10 and 11), which provides a way to determine the choice of model-free or model-based methods for different datasets for tractography in practice. For example, the model-free methods identify very few secondary and tertiary fibers for the WU-Minn-Ox HCP data with a maximum b-value of $3{,}000\ \mathrm{s/mm^2}$ while identify similar numbers of secondary and tertiary fibers compared to the model-based methods for the MGH-USC HCP data with a maximum b-value of $10{,}000\ \mathrm{s/mm^2}$. More interestingly, the distributions of the fiber crossing angles identified by the model-free and model-based methods were found to follow very different distributions in the WM on the same multi-shell data (Fig. 11) (Catani et al., 2012).

Cartesian q-space samples acquired in DSI could also benefit from GDSI's matrix formalism reconstruction. For example, the diffusion-encoding directions must be rotated to account for subject motion (Leemans and Jones, 2009) and gradient nonlinearity (Sotiropoulos et al., 2013), in which case the resultant q-space samples might no longer locate on a strict Cartesian grid. Errors will be introduced into the EAP if performing an FFT of the shifted samples. The shifted q-space samples could be interpolated back onto a Cartesian grid, but this requires extra computation. Applying GDSI's matrix formalism EAP reconstruction method directly to the shifted samples offers a more accurate and direct computation of the EAP.

DFT matrix reconstruction also allows the flexibility to recover the EAP at an arbitrary set of displacement directions and distances, e.g. on a Cartesian grid or on radial lines along multiple directions. Recovering the EAP on radial lines is useful for visualizing and analyzing the EAP. To the first point, a 3D EAP can be decomposed as a set of spherical functions at different displacement distances, which can be displayed using the

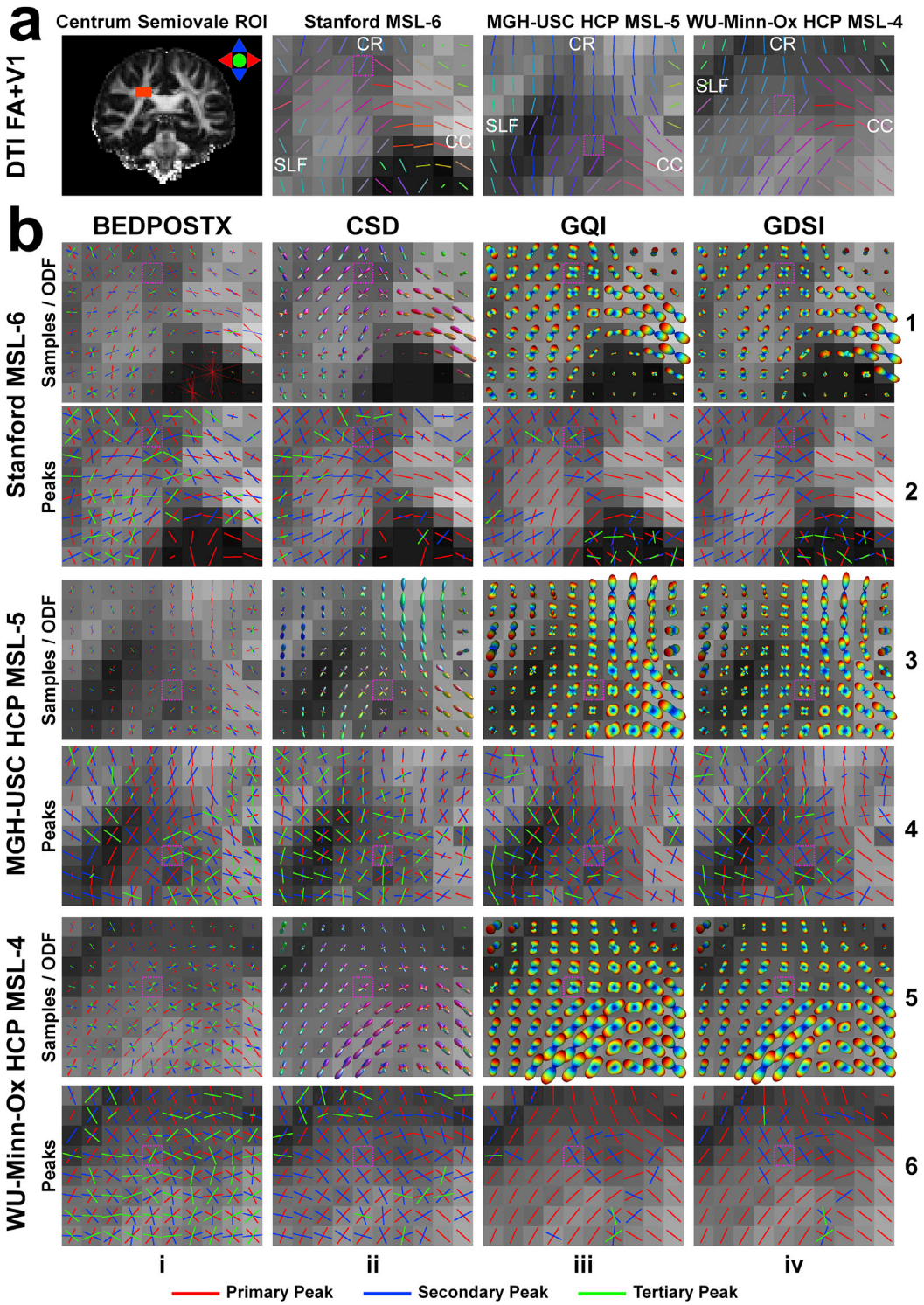

Fig. 10. Reconstructed fiber orientation samples (b, rows 1, 3, 5, columns i, 15 randomly selected samples, stick length proportional to the fiber volume fraction) and the average orientation (b, rows 2, 4, 6, columns i) from the BEDPOSTX method, and the orientation distribution function (ODF) (b, rows 1, 3, 5, columns ii-iv) and the ODF peaks (b, rows 2, 4, 6, columns ii-iv) from the multi-shell multi-tissue constrained spherical deconvolution (CSD) method, generalized q-space imaging (GQI), and the proposed generalized diffusion spectrum imaging (GDSI) method in the centrum semiovale region (a) from the Stanford (b, rows 1, 2), MGH-USC HCP (b, rows 3, 4) and WU-Minn-Ox HCP data (b, rows 5, 6). The primary eigenvectors (V1) from diffusion tensor imaging (DTI) are also depicted (a). All reconstruction results are displayed on top of the DTI fraction anisotropy (FA) map (windowed between 0 and 1). The diffusion ODF (b, rows 1, 3, 4, columns iii and iv) is color coded with the minimum as blue and the maximum as red. The red, blue and green vectors from the ODF peaks and BEDPOSTX (b, rows ii, iv, vi) represent the primary, secondary and tertiary diffusion orientations, respectively. DTI V1 and the fiber ODF (b, rows 1, 3, 4, columns ii) is color coded based on orientation (red: left-right, green: anterior-posterior, blue: superior-inferior). The centrum semiovale region contains intersection of the corpus callosum (CC), the corona radiata (CR), and the superior longitudinal fasciculus (SLF). The magenta dashed boxes indicate the crossing-fiber voxels presented in Figs. 5 and 9.

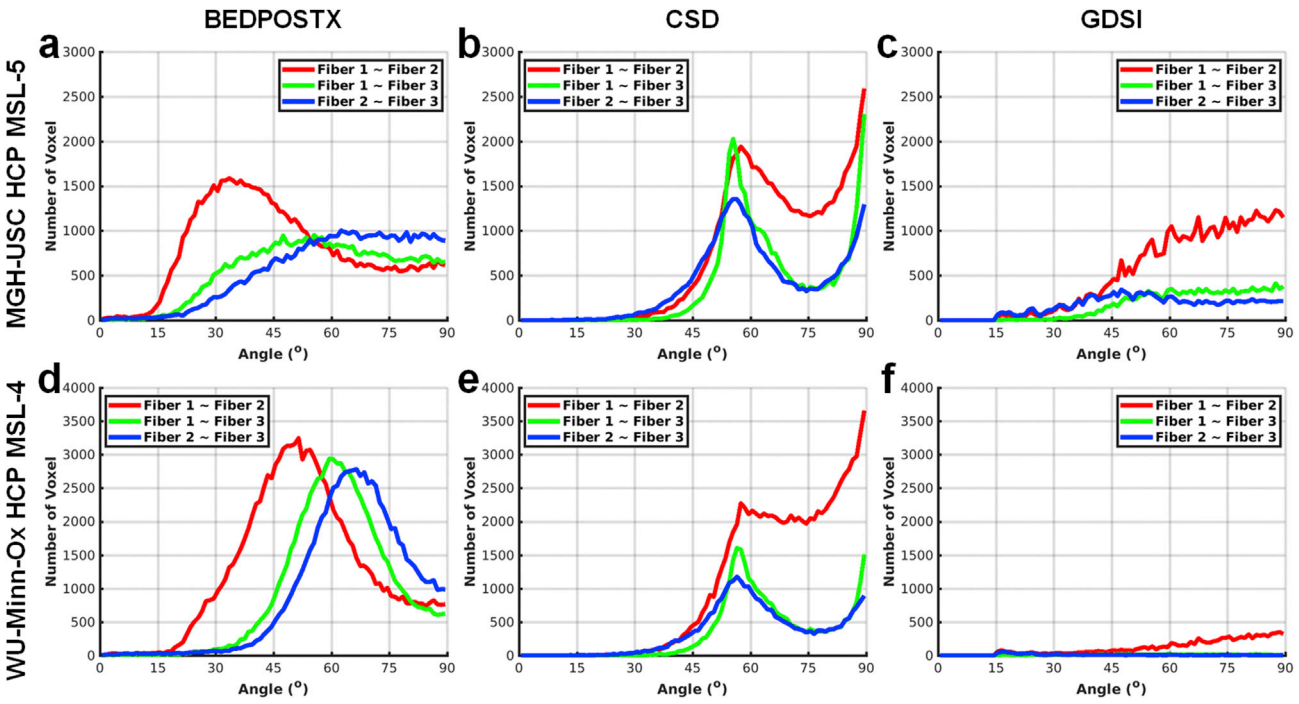

Fig. 11. Histograms of the angles between the primary, secondary and tertiary fiber orientations identified by the BEDPOSTX method (a, d), the multi-shell multi-tissue constrained spherical deconvolution (CSD) method (b, e), and the proposed generalized diffusion spectrum imaging (GDSI) method from the MGH-USC HCP (a–c) and WU-Minn-Ox HCP (d–f) multi-shell data. The histograms only include white matter voxels with both the primary and secondary fibers (red curves), both the primary and tertiary fibers (green curves) and both the secondary and tertiary fibers (blue curves). The area under the red, green and blue curves is equal to the number of the secondary fibers, tertiary fibers and tertiary fibers, respectively.

diffusion ODF visualization tools (Fig. 6 and supplementary videos). To the second point, there is no need to resample the EAP recovered from FFT-based reconstruction onto radial lines (as performed in DSI) to compute the diffusion ODF and many other orientation-specific EAP metrics (Figs. 7 and 8). Finally, along each radial line the EAP values beyond the first zero-crossing can be clipped to 0 to mitigate the Gibbs ringing, which results from the Fourier transform of the truncated q-space. The ringing can otherwise obscure the ODF shape and lead to erroneous fiber orientations (Figs. 3 and 4) (Paquette et al., 2016; Tian et al., 2016). In DSI, the negative lobes of the ringing present in the EAP are clipped to 0 to mitigate ringing.

A valid DFT matrix reconstruction on non-Cartesian, such as multi-shell, q-space sample requires uniform and sufficient q-space sampling density. However, the q-space sampling density is usually non-uniform. In multi-shell sampling, it is common to slightly under-sample the high q(b)-value regions (Fig. 4b). A sampling density correction is therefore needed to scale up the high q(b)-value signals, which contain high frequency information of the diffusion pattern. Here, we propose a fast geometrical method to estimate the q-space density correction factor that is similar to that used for image reconstruction of radial k-space samples (Pauly, 2005). This method makes an assumption that the q-space points are uniformly distributed on each shell, which is true for most multi-shell diffusion data, because of the requirement for uniform angular resolution. Advanced numerical methods such as using a 3D Voronoi diagram (Rasche et al., 1999) can be adopted for other q-space sampling patterns. The sampling density requirements for the multi-shell q-space sampling can be prescribed between shells (Appendix B Eq. (B2)) and within individual shell (Appendix B Eq. (B6)). These requirements have to be satisfied to avoid aliasing artifacts in the diffusion propagator reconstructed using GDSI (Tian et al., 2016; Tefera et al., 2013). For the multi-shell data used in this study, including those from the HCP, the sampling density requirements are satisfied. For under-sampled multi--shell data, a model-based approach or q-space compressed sensing techniques (Bilgic et al., 2012; Paquette et al., 2015) should be adopted.

In GDSI's matrix formalism, the mapping from the q-space signals to the diffusion ODF can be formulated as a linear system, which provides intuition on the diffusion ODF reconstruction. Specifically, the diffusion ODF value along a specific direction is a linear weighted summation of all the q-space samples, with the linear weights determined by the q-space location of the samples (Eq. (9) and Fig. 1). In the special case of the single-shell sampling, GDSI is consistent with QBI's use of the Funk-Radon transform that approximates the diffusion ODF value along a specific direction as the summation of the q-space signals along the orthogonal equator (Fig. 1e). Further, GDSI is equivalent to GQI in terms of ODF reconstruction if GQI's input signals are pre-compensated to account for q-space sampling non-uniformity. The difference of the two methods is that GQI solves the ODF analytically while GDSI solves the ODF using a matrix formalism. Compared to GQI, GDSI has the additional freedom to modify the EAP before ODF calculation (e.g. clipping the negative lobes of the ringing to 0 to mitigate ringing), and select the starting point (0 in GQI) (Paquette et al., 2016) and the power of displacement distance (0 and 2 in GQI) in the EAP integration for calculating the ODF, in addition to the benefit of recovering the EAP. GDSI unifies DSI, QBI and GQI in theory and can be used as a replacement in practice. GDSI's linear system formalism also allows decomposition of a diffusion ODF into a series of component ODFs from each q-space sampling point, or each q-space shell (Eq. (10), Figs. 3 and 9). This decomposition is potentially useful for protocol optimization.

In terms of computation, the matrix based reconstruction requires $N/\log(M)$ (N is the number of q-space signals, M is the number of EAP values) more multiplications and additions compared to the FFT-based reconstruction, but saves the computations of gridding multi-shell samples to the Cartesian grid and/or interpolating the EAP recovered on the Cartesian grid to radial lines to compute the ODF. N is relatively small for the q-space signals ($\sim 10^2$), in contrast to the number of k-space signals in a zero-padded 2D matrix ($\sim 10^4$). Further, the simple computation of multiplication and addition in the matrix based reconstruction can be easily accelerated via parallel computing and the use of graphics

processing units.

6. Summary

This study presents a generalized DSI framework named GDSI to recover the model-free spin displacement EAP from multi-shell diffusion MRI data. The proposed GDSI method involves correcting for the non-uniform q-space sampling density and performing the Fourier transform using a DFT matrix. GDSI is shown to produce the EAP and ODF that are in good agreement with those reconstructed from a full DSI acquisition, and to be broadly applicable to different types of multi-shell data including those from the HCP. The maps of EAP metrics such as P_r and r_α are demonstrated as additional means to characterize the diffusion patterns in different tissue types. GDSI also enables fiber orientations estimated from both the model-free and model-based methods on the same multi-shell data. Lastly, GDSI elucidates the contribution and combination of q-space samples to the diffusion ODF and relationship between various diffusion ODF reconstruction methods. In conclusion, our study provides a generalized DSI framework for recovering the EAP and ODF from Cartesian and multi-shell diffusion data, which contributes to the theoretical understanding of the DSI methodology, and flexibility of diffusion MRI data analysis for studying microstructure and connectivity in the human brain.

Acknowledgments

Data were provided in part by the Human Connectome Project, MGH-USC Consortium (Principal Investigators: Bruce R. Rosen, Arthur W. Toga and Van Wedeen; U01MH093765) funded by the NIH Blueprint Initiative for Neuroscience Research grant; the National Institutes of Health grant P41EB015896; and the Instrumentation Grants S10RR023043, 1S10RR023401, 1S10RR019307. Data were provided in part by the Human Connectome Project, WU-Minn Consortium (Principal Investigators: David Van Essen and Kamil Ugurbil; 1U54MH091657) funded by the 16 NIH Institutes and Centers that support the NIH Blueprint for Neuroscience Research; and by the McDonnell Center for Systems Neuroscience at Washington University. Funding was provided by the Wu Tsai Neurosciences Institute at Stanford, the Precision Health and Integrated Diagnostics Center at Stanford GE Healthcare, the Dana Foundation, the James S. McDonnell Foundation, the Gordon and Betty Moore Foundation, the Alfred P. Sloan Foundation, and National Institutes of Health: P41 EB015891, S10 RR026351, R01 NS095985, R01 MH111444, R21 MH116484, K23 NS094538 and F32 EY022294.

Appendix A

The dephasing term Φ of a spin is proportional to the scalar product between the applied gradient wave vector $\boldsymbol{q}$ ($=q\boldsymbol{v}$) and the relative spin displacement $\boldsymbol{r}$ ($=r\boldsymbol{u}$) as:

$$\Phi = 2\pi \boldsymbol{q}\boldsymbol{r} = 2\pi \cdot q\boldsymbol{v} \cdot r\boldsymbol{u}, \tag{A1}$$

where unit vectors $\boldsymbol{v}$ and $\boldsymbol{u}$ are directions of $\boldsymbol{q}$ and $\boldsymbol{r}$.

q can be expressed in terms of b for pulsed gradient waveform as:

$$q = \frac{1}{2\pi}\gamma g \delta = \frac{1}{2\pi}\sqrt{\frac{b}{\Delta - \frac{\delta}{3}}}, \tag{A2}$$

where Δ is the diffusion time, the interval between the two diffusion encoding gradient pulses during which spins are allowed to displace, and δ is the diffusion-encoding gradient strength. γ is the gyromagnetic ratio ($\gamma/2\pi = 42.58$ MHz/T). g is the diffusion-encoding gradient strength.

Any arbitrary displacement distance r can be expressed as a ratio λ of the mean displacement distance of free water (MDD_{water}) at 37 °C as:

$$r = \lambda \cdot MDD_{water}. \tag{A3}$$

For a specific diffusion pulse sequence with given Δ and δ, MDD_{water} is a constant number, which can be calculated using Einstein's equation (Einstein, 1905):

$$MDD = \sqrt{6D\left(\Delta - \frac{\delta}{3}\right)}, \tag{A4}$$

where D is the diffusion rate and Δ-$\delta/3$ is the effective diffusion time. MDD_{water} is equal to $\sqrt{6D_{water}\left(\Delta - \frac{\delta}{3}\right)}$, with the diffusion rate of free water at 37 °C $D_{\text{water}} = 2.5\times10^{-3}$ mm^2/s.

Substituting Equations (A2)-(A4) into Equation (A1) provides an expression for Φ in terms of the b-value, the b-vector and a ratio to the MDD_{water}:

$$\Phi = 2\pi \cdot \frac{1}{2\pi}\sqrt{\frac{b}{\Delta - \frac{\delta}{3}}}\boldsymbol{v} \cdot \lambda\sqrt{6D_{water}\left(\Delta - \frac{\delta}{3}\right)}\boldsymbol{u} = \sqrt{6D_{water}b}\boldsymbol{v} \cdot \lambda\boldsymbol{u}. \tag{A5}$$

Since the b-value (b) and the b-vector ($\boldsymbol{v}$) are commonly reported in most diffusion pulse sequences, it is more convenient to use Equation (A5) rather than Equation (A1).

Appendix B

The field of view determined by the q-space sampling density Δq should be larger than the extent of the ensemble average propagator (EAP) to avoid aliasing, as:

$$\frac{1}{\Delta q} \geq 2 \cdot MDD\,, \tag{B1}$$

where $2 \cdot MDD$ (mean displacement distance given in Eq. (A4)) is used to approximate the size of the EAP (Tian et al., 2016). The MDD of free water (MDD_{water}) can be used to provide an upper bound of the EAP size.

For the multi-shell q-space sampling, the sampling density should be sufficient between shells as well as within individual shell. For two arbitrary neighboring shells with b-values of b_1 and b_2 ($b_2 > b_1$), substituting Equations (A2) and (A4) into Equation (B1) gives:

$$\sqrt{b_2 \mathrm{D}} - \sqrt{b_1 \mathrm{D}} \leq \frac{\pi}{\sqrt{6}} \tag{B2}$$

where D is the diffusion coefficient. For an approximate higher bound of the apparent diffusion coefficient in the *in vivo* human brain of $D = 1.7 \times 10^{-3}\,\mathrm{mm}^2/\mathrm{s}$ (the apparent diffusion coefficient along the primary fiber orientation in the corpus callosum measured by DTI (Pierpaoli et al., 1996; Tian et al., 2016), the b-value requirement specified in Equation (B2) is simplified as:

$$\sqrt{b_2} - \sqrt{b_1} \leq 31, \tag{B3}$$

where the unit of b_1 and b_2 is $\mathrm{s/mm}^2$.

On a specific shell with q-value q (b-value b) and N uniformly distributed samples, each sample has a solid angle of $A = 4\pi/N$. The solid angle of a sample is also geometrically (Figure Appendix B) determined as:

$$A = 2\pi(1 - \cos\theta). \tag{B4}$$

The distance between any two samples (ac = bd in Figure Appendix B) on the shell is given by:

$$\Delta q = 2 \cdot q \sin\theta. \tag{B5}$$

Substituting Equations (A2), (A4), (B4) and (B5) into Equation (B1) gives:

$$bD \leq \frac{\pi^2}{96\left(\frac{1}{N} - \frac{1}{N^2}\right)}. \tag{B6}$$

For $D = 1.7 \times 10^{-3}\,\mathrm{mm}^2/\mathrm{s}$ and assuming $\frac{1}{N^2}$ is negligible (since $\frac{1}{N} \gg \frac{1}{N^2}$), the number of samples N on a shell should satisfy:

$$N \geq \frac{b}{60}, \tag{B7}$$

where b-value has a unit of $\mathrm{s/mm}^2$.

The diffusion coefficient D in Equations (B2) and (B6) should adapt to different applications accordingly. For example, the apparent diffusion coefficient is as high as $\sim 2.5 \times 10^{-3}\,\mathrm{mm}^2/\mathrm{s}$ for some types of tumor (Yamasaki et al., 2005) while about $10\times$ lower in the *ex vivo* brain tissue compared to in the *in vivo* brain (Tian et al., 2016).

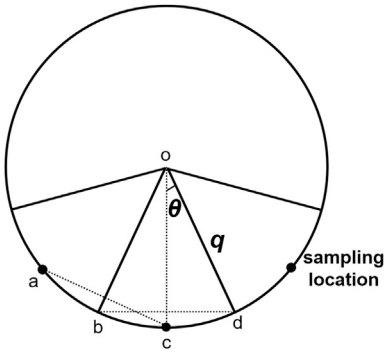

Fig. Appendix B. A 2D illustration of a q-space sampling shell of q-value q. Radial lines ob and od define the cone associated with the q-space sample c. The distance between two samples (ac) is equal to the distance bd ($=2 \cdot q\sin\theta$).

Appendix C. Supplementary data

Supplementary data to this article can be found online at https://doi.org/10.1016/j.neuroimage.2019.01.038.

References

Aboitiz, F., Scheibel, A.B., Fisher, R.S., Zaidel, E., 1992. Fiber composition of the human corpus callosum. Brain Res. 598 (1), 143–153.

Aganj, I., Lenglet, C., Sapiro, G., Yacoub, E., Ugurbil, K., Harel, N., 2010. Reconstruction of the orientation distribution function in single-and multiple-shell q-ball imaging within constant solid angle. Magn. Reson. Med. 64 (2), 554–566.

Andersson, J.L., Sotiropoulos, S.N., 2016. An integrated approach to correction for off-resonance effects and subject movement in diffusion MR imaging. Neuroimage 125, 1063–1078.
Andersson, J.L., Skare, S., Ashburner, J., 2003. How to correct susceptibility distortions in spin-echo echo-planar images: application to diffusion tensor imaging. Neuroimage 20 (2), 870–888.
Assaf, Y., Cohen, Y., 1999. Structural information in neuronal tissue as revealed by q-space diffusion NMR spectroscopy of metabolites in bovine optic nerve. NMR Biomed. 12 (6), 335–344.
Assaf, Y., Cohen, Y., 2000. Assignment of the water slow-diffusing component in the central nervous system using q-space diffusion MRS: implications for fiber tract imaging. Magn. Reson. Med. 43 (2), 191–199.
Assaf, Y., Mayk, A., Cohen, Y., 2000. Displacement imaging of spinal cord using q-space diffusion-weighted MRI. Magn. Reson. Med. 44 (5), 713–722.
Assaf, Y., Ben-Bashat, D., Chapman, J., Peled, S., Biton, I.E., Kafri, M., et al., 2002. High b-value q-space analyzed diffusion-weighted MRI: application to multiple sclerosis. Magn. Reson. Med. 47 (1), 115–126.
Assaf, Y., Chapman, J., Ben-Bashat, D., Hendler, T., Segev, Y., Korczyn, A.D., et al., 2005. White matter changes in multiple sclerosis: correlation of q-space diffusion MRI and 1 H. MRS. Magn. Reson. Imag. 23 (6), 703–710.
Assemlal, H.-E., Tschumperlé, D., Brun, L., 2009. Efficient and robust computation of PDF features from diffusion MR signal. Med. Image Anal. 13 (5), 715–729.
Assemlal, H.E., Campbell, J., Pike, B., Siddiqi, K., 2011. Apparent intravoxel fibre population dispersion (FPD) using spherical harmonics. In: Proceedings of the International Conference on Medical Image Computing and Computer-Assisted Intervention, vol. 6892. Springer, Berlin, Heidelberg, pp. 157–165. Lecture Notes in Computer Science.
Baete, S.H., Boada, F.E., 2018. Accelerated radial diffusion spectrum imaging using a multi-echo stimulated echo diffusion sequence. Magn. Reson. Med. 79 (1), 306–316.
Baete, S.H., Yutzy, S., Boada, F.E., 2016. Radial q-space sampling for DSI. Magn. Reson. Med. 76 (3), 769–780.
Basser, P.J., Mattiello, J., LeBihan, D., 1994. MR diffusion tensor spectroscopy and imaging. Biophys. J. 66 (1), 259–267.
Beatty, P.J., Nishimura, D.G., Pauly, J.M., 2005. Rapid gridding reconstruction with a minimal oversampling ratio. IEEE Trans. Med. Imag. 24 (6), 799–808.
Behrens, T., Woolrich, M., Jenkinson, M., Johansen-Berg, H., Nunes, R., Clare, S., et al., 2003. Characterization and propagation of uncertainty in diffusion-weighted MR imaging. Magn. Reson. Med. 50 (5), 1077–1088.
Bilgic, B., Setsompop, K., Cohen-Adad, J., Yendiki, A., Wald, L.L., Adalsteinsson, E., 2012. Accelerated diffusion spectrum imaging with compressed sensing using adaptive dictionaries. Magn. Reson. Med. 68 (6), 1747–1754.
Callaghan, P.T., 1991. Principles of Nuclear Magnetic Resonance Microscopy. Clarendon Press, Oxford.
Callaghan, P., 1996. NMR imaging, NMR diffraction and applications of pulsed gradient spin echoes in porous media. Magn. Reson. Imaging 14 (7), 701–709.
Callaghan, P.T., 2011. Translational Dynamics and Magnetic Resonance: Principles of Pulsed Gradient Spin Echo NMR. Oxford University Press.
Callaghan, P.T., Eccles, C.D., Xia, Y., 1988. NMR microscopy of dynamic displacements - k-space and q-space imaging. J. Phys. E Sci. Instrum. 21 (8), 820–822.
Canales-Rodríguez, E.J., Lin, C.-P., Iturria-Medina, Y., Yeh, C.-H., Cho, K.-H., Melie-García, L., 2010. Diffusion orientation transform revisited. Neuroimage 49 (2), 1326–1339.
Canales-Rodríguez, E.J., Iturria-Medina, Y., Alemán-Gómez, Y., Melie-García, L., 2010. Deconvolution in diffusion spectrum imaging. Neuroimage 50 (1), 136–149.
Catani, M., Bodi, I., Dell'Acqua, F., 2012. Comment on "The geometric structure of the brain fiber pathways. Science 337 (6102), 1605.
Cohen, Y., Assaf, Y., 2002. High b-value q-space analyzed diffusion-weighted MRS and MRI in neuronal tissues–a technical review. NMR Biomed. 15 (7-8), 516–542.
Conturo, T.E., Lori, N.F., Cull, T.S., Akbudak, E., Snyder, A.Z., Shimony, J.S., et al., 1999. Tracking neuronal fiber pathways in the living human brain. Proc. Natl. Acad. Sci. Unit. States Am. 96 (18), 10422–10427.
Cory, D., 1990. Measurement of translational displacement probabilities by NMR: an indicator of compartmentation. Magn. Reson. Med. 14 (3), 435–444.
Dale, A.M., Fischl, B., Sereno, M.I., 1999. Cortical surface-based analysis: I. Segmentation and surface reconstruction. Neuroimage 9 (2), 179–194.
Descoteaux, M., Deriche, R., Le Bihan, D., Mangin, J.F., Poupon, C., 2009. Diffusion propagator imaging: using Laplace's equation and multiple shell acquisitions to reconstruct the diffusion propagator. In: Proceedings of the International Conference on Information Processing in Medical Imaging, vol. 5636. Springer, Berlin, Heidelberg, pp. 1–13. Lecture Notes in Computer Science.
Descoteaux, M., Deriche, R., Le Bihan, D., Mangin, J.-F., Poupon, C., 2011. Multiple q-shell diffusion propagator imaging. Med. Image Anal. 15 (4), 603–621.
Edlow, B.L., Haynes, R.L., Takahashi, E., Klein, J.P., Cummings, P., Benner, T., et al., 2013. Disconnection of the ascending arousal system in traumatic coma. J. Neuropathol. Exp. Neurol. 72 (6), 505–523.
Edlow, B.L., Copen, W.A., Izzy, S., Kouwe, A., Glenn, M.B., Greenberg, S.M., et al., 2016. Longitudinal diffusion tensor imaging detects recovery of fractional anisotropy within traumatic axonal injury lesions. Neurocritical Care 24 (3), 342–352.
Eichner, C., Cauley, S.F., Cohen-Adad, J., Möller, H.E., Turner, R., Setsompop, K., et al., 2015. Real diffusion-weighted MRI enabling true signal averaging and increased diffusion contrast. Neuroimage 122, 373–384.
Einstein, A., 1905. Über die von der molekularkinetischen Theorie der Wärme geforderte Bewegung von in ruhenden Flüssigkeiten suspendierten Teilchen. Ann. Phys. 322 (8), 549–560.
Fan, Q., Nummenmaa, A., Witzel, T., Zanzonico, R., Keil, B., Cauley, S., et al., 2014. Investigating the capability to resolve complex white matter structures with high b-value diffusion magnetic resonance imaging on the MGH-USC connectom scanner. Brain Connect. 4 (9), 718–726.
Fan, Q., Witzel, T., Nummenmaa, A., Van Dijk, K.R., Van Horn, J.D., Drews, M.K., et al., 2016. MGH–USC Human Connectome Project datasets with ultra-high b-value diffusion MRI. Neuroimage 124, 1108–1114.
Farrell, J.A., Zhang, J., Jones, M.V., DeBoy, C.A., Hoffman, P.N., Landman, B.A., et al., 2010. q-space and conventional diffusion imaging of axon and myelin damage in the rat spinal cord after axotomy. Magn. Reson. Med. 63 (5), 1323–1335.
Fatima, Z., Motosugi, U., Hori, M., Onodera, T., Ishigame, K., Yagi, K., et al., 2013. Age-related white matter changes in high b-value q-space diffusion-weighted imaging. Neuroradiology 55 (3), 253–259.
Fischl, B., Dale, A.M., 2000. Measuring the thickness of the human cerebral cortex from magnetic resonance images. Proc. Natl. Acad. Sci. Unit. States Am. 97 (20), 11050–11055.
Fujiyoshi, K., Hikishima, K., Nakahara, J., Tsuji, O., Hata, J., Konomi, T., et al., 2016. Application of q-space diffusion MRI for the visualization of white matter. J. Neurosci. 36 (9), 2796–2808.
Garyfallidis, E., Brett, M., Amirbekian, B., Rokem, A., Van Der Walt, S., Descoteaux, M., Nimmo-Smith, I., 2014. Dipy, a library for the analysis of diffusion MRI data. Frontiers in Neuroinf. 8, 8.
Guo, F., Parker, G., De Luca, A., Jones, D., Viergever, M., Leemans, A., Tax, C.M., 2018. The influence of gradient nonlinearity on spherical deconvolution approaches: to correct or not to correct? Proc. Intl. Soc. Mag. Reson. Med. 26, 1591.
Hoffman, M.P., Taylor, E.N., Aninwene, G.E., Sadayappan, S., Gilbert, R.J., 2018. Assessing the multiscale architecture of muscular tissue with Q-space magnetic resonance imaging. Microsc. Res. Tech. 81 (2), 162–170.
Hori, M., Yoshida, M., Yokoyama, K., Kamagata, K., Kumagai, F., Fukunaga, I., et al., 2014. Multiple sclerosis: benefits of q-space imaging in evaluation of normal-appearing and periplaque white matter. Magn. Reson. Imaging 32 (6), 625–629.
Hori, M., Kamiya, K., Nakanishi, A., Fukunaga, I., Miyajima, M., Nakajima, M., et al., 2016. Prospective estimation of mean axon diameter and extra-axonal space of the posterior limb of the internal capsule in patients with idiopathic normal pressure hydrocephalus before and after a lumboperitoneal shunt by using q-space diffusion MRI. Eur. Radiol. 26 (9), 2992–2998.
Hosseinbor, A.P., Chung, M.K., Wu, Y.-C., Alexander, A.L., 2013. Bessel fourier orientation reconstruction (bfor): an analytical diffusion propagator reconstruction for hybrid diffusion imaging and computation of q-space indices. Neuroimage 64, 650–670.
Huber, E., Donnelly, P.M., Rokem, A., Yeatman, J.D., 2018. Rapid and widespread white matter plasticity during an intensive reading intervention. Nat. Commun. 9 (1), 2260.
Jenkinson, M., Beckmann, C.F., Behrens, T.E.J., Woolrich, M.W., Smith, S.M., 2012. FSL. NeuroImage. 62 (2), 782–790.
Jenner, C., Xia, Y., Eccles, C., Callaghan, P., 1988. Circulation of water within wheat grain revealed by nuclear magnetic resonance micro-imaging. Nature 336, 399–402.
Jeurissen, B., Tournier, J.-D., Dhollander, T., Connelly, A., Sijbers, J., 2014. Multi-tissue constrained spherical deconvolution for improved analysis of multi-shell diffusion MRI data. Neuroimage 103, 411–426.
Kamath, A., Aganj, I., Xu, J., Yacoub, E., Ugurbil, K., Sapiro, G., et al. (Eds.), 2012. Generalized Constant Solid Angle Odf and Optimal Acquisition Protocol for Fiber Orientation Mapping. MICCAI Workshop on Computational Diffusion MRI.
Kamiya, K., Hori, M., Miyajima, M., Nakajima, M., Suzuki, Y., Kamagata, K., et al., 2014. Axon diameter and intra-axonal volume fraction of the corticospinal tract in idiopathic normal pressure hydrocephalus measured by q-space imaging. PLoS One 9 (8) e103842.
Kärger, J., Heink, W., 1969. The propagator representation of molecular transport in microporous crystallites. J. Magn. Reson. 51 (1), 1–7, 1983.
King, M.D., Houseman, J., Roussel, S.A., Van Bruggen, N., Williams, S.R., Gadian, D.G., 1994. q-Space imaging of the brain. Magn. Reson. Med. 32 (6), 707–713.
King, M.D., Houseman, J., Gadian, D., Connelly, A., 1997. Localized q-space imaging of the mouse brain. Magn. Reson. Med. 38 (6), 930–937.
Leemans, A., Jones, D.K., 2009. The B-matrix must be rotated when correcting for subject motion in DTI data. Magn. Reson. Med. 61 (6), 1336–1349.
Lin, C.-P., Wedeen, V.J., Chen, J.-H., Yao, C., Tseng, W.-Y.I., 2003. Validation of diffusion spectrum magnetic resonance imaging with manganese-enhanced rat optic tracts and ex vivo phantoms. Neuroimage 19 (3), 482–495.
Ljunggren, S., 1969. A simple graphical representation of Fourier-based imaging methods. J. Magn. Reson. 54 (2), 338–343, 1983.
McNab, J.A., Edlow, B.L., Witzel, T., Huang, S.Y., Bhat, H., Heberlein, K., et al., 2013. The Human Connectome Project and beyond: initial applications of 300 mT/m gradients. Neuroimage 80, 234–245.
Mesri, H.Y., David, S., Viergever, M.A., Leemans, A.A., 2018. Investigating the effect of gradient nonlinearities on diffusional kurtosis imaging parameters: results from the Human Connectome Project. Proc. Intl. Soc. Mag. Reson. Med. 26, 1647.
Mitra, P.P., Halperin, B.I., 1995. Effects of finite gradient-pulse widths in pulsed-field-gradient diffusion measurements. J. Magn. Reson. Ser. A 113 (1), 94–101.
Mitra, P.P., Latour, L., Kleinberg, R.L., Sotak, C.H., 1995. Pulsed-field-gradient NMR measurements of restricted diffusion and the return-to-the-origin probability. J. Magn. Reson. Ser. A 114 (1), 47–58.
Mori, S., Crain, B.J., Chacko, V., Van Zijl, P., 1999. Three-dimensional tracking of axonal projections in the brain by magnetic resonance imaging. Ann. Neurol. 45 (2), 265–269.
Ong, H.H., Wehrli, F.W., 2010. Quantifying axon diameter and intra-cellular volume fraction in excised mouse spinal cord with q-space imaging. Neuroimage 51 (4), 1360–1366.

Ong, H.H., Wright, A.C., Wehrli, S.L., Souza, A., Schwartz, E.D., Hwang, S.N., et al., 2008. Indirect measurement of regional axon diameter in excised mouse spinal cord with q-space imaging: simulation and experimental studies. Neuroimage 40 (4), 1619–1632.
Özarslan, E., Shepherd, T.M., Vemuri, B.C., Blackband, S.J., Mareci, T.H., 2006. Resolution of complex tissue microarchitecture using the diffusion orientation transform (DOT). Neuroimage 31 (3), 1086–1103.
Özarslan, E., Koay, C.G., Shepherd, T.M., Komlosh, M.E., İrfanoğlu, M.O., Pierpaoli, C., et al., 2013. Mean apparent propagator (MAP) MRI: a novel diffusion imaging method for mapping tissue microstructure. Neuroimage 78, 16–32.
Paquette, M., Merlet, S., Gilbert, G., Deriche, R., Descoteaux, M., 2015. Comparison of sampling strategies and sparsifying transforms to improve compressed sensing diffusion spectrum imaging. Magn. Reson. Med. 73 (1), 401–416.
Paquette, M., Gilbert, G., Descoteaux, M., 2016. Optimal DSI reconstruction parameter recommendations: better ODFs and better connectivity. Neuroimage 142, 1–13.
Pauly, J., 2005. Non-Cartesian Reconstruction. Stanford EE369C Lecture Notes.
Pierpaoli, C., Jezzard, P., Basser, P.J., Barnett, A., Di Chiro, G., 1996. Diffusion tensor MR imaging of the human brain. Radiology 201 (3), 637–648.
Rasche, V., Proksa, R., Sinkus, R., Bornert, P., Eggers, H., 1999. Resampling of data between arbitrary grids using convolution interpolation. IEEE Trans. Med. Imag. 18 (5), 385–392.
Setsompop, K., Kimmlingen, R., Eberlein, E., Witzel, T., Cohen-Adad, J., McNab, J.A., et al., 2013. Pushing the limits of in vivo diffusion MRI for the human connectome project. Neuroimage 80, 220–233.
Smith, S.M., Jenkinson, M., Woolrich, M.W., Beckmann, C.F., Behrens, T.E., Johansen-Berg, H., et al., 2004. Advances in functional and structural MR image analysis and implementation as FSL. Neuroimage 23, S208–S219.
Sotiropoulos, S.N., Jbabdi, S., Xu, J., Andersson, J.L., Moeller, S., Auerbach, E.J., et al., 2013. Advances in diffusion MRI acquisition and processing in the human connectome Project. Neuroimage 80, 125–143.
Stejskal, E., 1965. Use of spin echoes in a pulsed magnetic-field gradient to study anisotropic, restricted diffusion and flow. J. Chem. Phys. 43 (10), 3597–3603.
Stejskal, E., Tanner, J., 1965. Spin diffusion measurements: spin echoes in the presence of a time-dependent field gradient. J. Chem. Phys. 42 (1), 288–292.
Tanikawa, M., Nakahara, J., Hata, J., Suzuki, S., Fujiyoshi, K., Fujiwara, H., et al., 2017. q-Space Myelin Map imaging for longitudinal analysis of demyelination and remyelination in multiple sclerosis patients treated with fingolimod: a preliminary study. J. Neurol. Sci. 373, 352–357.
Taylor, E.N., Hoffman, M.P., Aninwene, G.E., Gilbert, R.J., 2015. Patterns of intersecting fiber arrays revealed in whole muscle with generalized Q-space imaging. Biophys. J. 108 (11), 2740–2749.
Taylor, E.N., Ding, Y., Zhu, S., Cheah, E., Alexander, P., Lin, L., et al., 2017. Association between tumor architecture derived from generalized Q-space MRI and survival in glioblastoma. Oncotarget 5.
Tefera, G.B., Zhou, Y., Juneja, V., Narayana, P.A., 2013. Evaluation of fiber tracking from subsampled q-space data in diffusion spectrum imaging. Magn. Reson. Imaging 31 (6), 820–826.
Tian, Q., Rokem, A., Folkerth, R.D., Nummenmaa, A., Fan, Q., Edlow, B.L., McNab, J.A., 2016. Q-space truncation and sampling in diffusion spectrum imaging. Magn. Reson. Med. 76 (6), 1750–1763.
Tian, Q., Yang, G., Leuze, C.W., Rokem, A., Edlow, B.L., McNab, J.A., 2017a. A comprehensive analytic solution of diffusion orientation distribution function. In: In the Annual Meeting of the Organization for Human Brain Mapping (OHBM).
Tian, Q., Yang, G., Leuze, C.W., Rokem, A., Edlow, B.L., McNab, J.A., 2017b. Model-free Fourier reconstruction of the diffusion propagator from multi-b-shell diffusion data. Proc. Intl. Soc. Mag. Reson. Med. 25, 3528.
Tournier, J.D., Calamante, F., Gadian, D.G., Connelly, A., 2004. Direct estimation of the fiber orientation density function from diffusion-weighted MRI data using spherical deconvolution. Neuroimage 23 (3), 1176–1185.
Tournier, J.D., Calamante, F., Connelly, A., 2007. Robust determination of the fibre orientation distribution in diffusion MRI: non-negativity constrained super-resolved spherical deconvolution. Neuroimage 35 (4), 1459–1472.
Tuch, D.S., 2004. Q-ball imaging. Magn. Reson. Med. 52 (6), 1358–1372.
Twieg, D.B., 1983. The k-trajectory formulation of the NMR imaging process with applications in analysis and synthesis of imaging methods. Med. Phys. 10 (5), 610–621.
Ugurbil, K., Xu, J., Auerbach, E.J., Moeller, S., Vu, A.T., Duarte-Carvajalino, J.M., et al., 2013. Pushing spatial and temporal resolution for functional and diffusion MRI in the Human Connectome Project. Neuroimage 80, 80–104.
Vaillancourt, O., Chamberland, M., Houde, J.C., Descoteaux, M., 2015. Visualization of diffusion propagator and multiple parameter diffusion signal. In: Proceedings of the Visualization and Processing of Higher Order Descriptors for Multi-Valued Data. Springer, Cham, pp. 191–212. Mathematics and Visualization.
van der Kouwe, A.J., Benner, T., Salat, D.H., Fischl, B., 2008. Brain morphometry with multiecho MPRAGE. Neuroimage 40 (2), 559–569.
Van Essen, D.C., Smith, S.M., Barch, D.M., Behrens, T.E., Yacoub, E., Ugurbil, K., 2013. The Wu-Minn human connectome Project: an overview. Neuroimage 80, 62–79.
Wedeen, V.J., Reese, T.G., Tuch, D.S., Weigel, M.R., Dou, J.G., Weiskoff, R.M., Chessler, D., 2000. Mapping fiber orientation spectra in cerebral white matter with Fourier-transform diffusion MRI. Proc. Intl. Sot. Mag. Reson. Med. 8, 82.
Wedeen, V.J., Hagmann, P., Tseng, W.Y.I., Reese, T.G., Weisskoff, R.M., 2005. Mapping complex tissue architecture with diffusion spectrum magnetic resonance imaging. Magn. Reson. Med. 54 (6), 1377–1386.
Wedeen, V.J., Rosene, D.L., Wang, R., Dai, G., Mortazavi, F., Hagmann, P., et al., 2012. The geometric structure of the brain fiber pathways. Science 335 (6076), 1628–1634.
Wiegell, M.R., Reese, T., Tuch, D.S., Sorensen, A.G., Wedeen, V.J., 2001. Diffusion spectrum imaging of fiber white matter degeneration. Proc. Int. Soc. Mag. Reson. Med. 9, 504.
Wu, Y.-C., Alexander, A.L., 2007. Hybrid diffusion imaging. Neuroimage 36 (3), 617–629.
Wu, Y.-C., Field, A.S., Alexander, A.L., 2008. Computation of diffusion function measures in q-space using magnetic resonance hybrid diffusion imaging. Med. Imag. IEEE Trans. 27 (6), 858–865.
Yamada, I., Hikishima, K., Miyasaka, N., Tokairin, Y., Ito, E., Kawano, T., et al., 2015. Esophageal carcinoma: evaluation with q-space diffusion-weighted MR imaging ex vivo. Magn. Reson. Med. 73 (6), 2262–2273.
Yamasaki, F., Kurisu, K., Satoh, K., Arita, K., Sugiyama, K., Ohtaki, M., et al., 2005. Apparent diffusion coefficient of human brain tumors at MR imaging. Radiology 235 (3), 985–991.
Yeatman, J.D., Dougherty, R.F., Myall, N.J., Wandell, B.A., Feldman, H.M., 2012. Tract profiles of white matter properties: automating fiber-tract quantification. PLoS One 7 (11), e49790.
Yeatman, J.D., Richie-Halford, A., Smith, J.K., Keshavan, A., Rokem, A., 2018. A browser-based tool for visualization and analysis of diffusion MRI data. Nat. Commun. 9 (1), 940.
Yeh, F.-C., Wedeen, V.J., Tseng, W., 2010. Generalized q-sampling imaging. IEEE Trans. Med. Imag. 29 (9), 1626.
Zhang, H., Schneider, T., Wheeler-Kingshott, C.A., Alexander, D.C., 2012. NODDI: practical in vivo neurite orientation dispersion and density imaging of the human brain. Neuroimage 61 (4), 1000–1016.